Sensitivity of the Atlantic meridional overturning circulation and climate to tropical Indian Ocean warming

Brady Ferster, Alexey V. Fedorov, Juliette Mignot, Éric Guilyardi

Sensitivity of the Atlantic meridional overturning circulation and climate to tropical Indian Ocean warming

Brady S. Ferster[1], Alexey V. Fedorov[1,2], Juliette Mignot[1], Eric Guilyardi[1,3]

[1]LOCEAN-IPSL (Sorbonne Université, CNRS, IRD, MNHN), Paris, France.
[2]Department of Earth and Planetary Sciences, Yale University, New Haven, CT, USA.
[3]NCAS-Climate, University of Reading, Reading, UK.

Corresponding author: Brady S. Ferster (brady.ferster@locean.ipsl.fr)

Abstract

A salient feature of anthropogenic climate change is the enhanced warming of the tropical Indian Ocean (TIO) relative to the tropics. Recent studies show that this warming can remotely modulate the Atlantic meridional overturning circulation (AMOC). Motivated by these results, we systematically study the sensitivity of the AMOC and Atlantic climate to changes in TIO temperature using the latest coupled climate model from the Institut Pierre Simon Laplace (IPSL-CM6A-LR). Ensemble experiments nudging the TIO surface temperatures by -2°C, -1°C, +1°C, and +2°C are conducted. Within a few years after the forcing is imposed, different atmospheric teleconnections begin to drive the AMOC "fast" and "slow" responses, yielding after 150 years an AMOC equilibrium sensitivity of about +9.4 Sv per 1°C of relative TIO warming. A water mass transformation analysis shows that the fast response to TIO warming (on decadal timescales) is largely driven by surface cooling in the Labrador Sea caused by an induced positive North Atlantic Oscillation (NAO)-like mean pattern. By contrast, the slow response (on multi-decadal to centennial timescales) is driven by the gradual advection of positive salinity anomalies from the tropical Atlantic, which predominantly affect the Nordic Seas. The response is non-linear in that a TIO warming strengthens the AMOC through increase in Labrador Sea deep water formation, while a TIO cooling slows down the AMOC via sea ice expansion over the Nordic Seas deep-water formation region, ultimately leading to the AMOC shut-down in the -2ºC-TIO experiment. These results help understand the role of interbasin connections and AMOC drivers in a warming climate.

Keywords AMOC, North Atlantic, Teleconnections, North Atlantic Oscillation, Indian ocean warming, Arctic sea ice

1. Introduction

The North Atlantic plays a fundamental role in Earth's climate, providing a pathway for the northward transport of energy (heat). Through the upper branch of the Atlantic meridional overturning circulation (AMOC), heat is transported to the high-latitudes, where surface waters lose buoyancy, forming deep-water that feeds the southward return flow of the overturning cell. The AMOC exhibits low-frequency variability, making it important for climate prediction and understanding past climates (for a recent review see Buckley and Marshall, 2016). For example, AMOC variability has been shown to influence the latitudinal position of the Intertropical Convergence Zone (e.g. Vellinga and Wood, 2002), seasonal weather patterns over the Northern Hemisphere (Sutton and Hodson, 2005; Woollings et al., 2012; Liu et al. 2020), sea-level rise (Hu et al., 2011), and ocean carbon (CO_2) sequestration (Sabine et al., 2004). Observations from the RAPID Climate Change–Meridional Overturning Circulation and Heatflux Array (RAPID–MOCHA) at 26°N have highlighted strong interannual variability since 2008 (Smeed et al., 2018). Whether the AMOC has been declining as part of climate changes is a subject of ongoing debate (e.g. Worthington et al. 2021; Caesar et al 2021). For instance, the latter study has used proxy reconstructions of the AMOC to suggest that the AMOC over the last 50 years is at an unprecedented weak state since 1000 years. The Coupled Model Intercomparison Project phase 5 (CMIP5) predicts a reduced AMOC state under the influence of anthropogenic forcing (Chang et al., 2013; Rahmstorf et al., 2015) with an average decline of 1 Sv per decade (IPCC, 2013). The impacts of declining AMOC under global warming are summarized in Liu et al. (2020).

Overall, there remains a large uncertainty on the magnitude and timing of the future AMOC decline as the AMOC sensitivity to climate forcing strongly depends on the model and the CO_2 scenario used. The AMOC can also respond to teleconnections from other regions. Accordingly, the goal of this study is to conduct a systematic investigation of the sensitivity of

61 the AMOC to changes in the tropical Indian ocean temperature. This is motivated by the
62 observations of the past several decades of the enhanced warming of the tropical Indian Ocean
63 (TIO) relative to the rest of the global ocean and, in particular, relative to the tropical Atlantic
64 and Pacific (Du & Xie, 2008; Dong and Zhou, 2014). In satellite-derived observations, the TIO
65 is estimated to be warming by 0.05°C per decade faster than the tropical Atlantic and Pacific
66 between 1950 and 2015 (Hu and Fedorov, 2019; hereafter HF19). The TIO has been observed
67 to be warming faster than the Atlantic and Pacific; the warming is largley attributed to
68 influences of greenhouse gases, although the exact mechanism of the enhanced warming is not
69 fully explained from the increased surface heat flux and ocean transports (ocean-atmosphere
70 feedbacks may be important; Rao et al., 2012; Roxy et al., 2014).

71 To quantify the impact of changes in the TIO, we consider TIO warming relative to the
72 whole tropical ocean (rTIO), as this parameter is thought to drive dynamic and thermodynamic
73 responses and initiate global teleconnections and large-scale patterns (HF19). In other words,
74 we ignore the case when the Indian and Pacific Ocean would warm at the same rate. The rTIO
75 warming increases latent heat release in the atmosphere over the Indian Ocean, which induces
76 atmospheric equatorial Kelvin and Rossby waves, as well as extra-tropical Rossby wave trains
77 propagating from the tropics to high latitudes (Trenberth et al., 1998, HF19). The resulting
78 wave propagation can affect the tropical Atlantic and high-latitude Atlantic, respectively (Hu
79 and Fedorov, 2020; hereafter HF20).

80 On a monthly timescale, a quasi-stationary Rossby wave train traveling from the
81 anomalously warm Indian ocean reaches the mid- to high-latitude North Atlantic and induces
82 a positive North Atlantic Oscillation (NAO)-like pattern (Hoerling et al., 2001; 2004; Bader &
83 Latif, 2003; 2005; Baker et al., 2019; HF19), increasing the subpolar westerlies (Hurrell, 1995;
84 HF20) and thereby modulating oceanic heat loss to the atmosphere (Lee et al., 2011) within
85 the North Atlantic. On similar timescales, a warm rTIO induces an atmospheric Gill-type

response in the Tropics (Matsuno 1966 and Gill 1980) with pronounced stationary Rossby and Kelvin waves, and the latter strengthen the Walker Cells in the Pacific and Atlantic. This teleconnection typically leads to increased evaporative cooling and decreased precipitation (hence increased salinity) throughout the tropical Atlantic (HF19).

The rTIO has strong effects on the tropical Pacific and Atlantic (HF19), which may result in an uneven distribution of energy between the hemispheres and a migration of the ITCZ to compensate the imbalance (Vellinga & Wu, 2004; Frierson et al., 2013; Marshall et al., 2014; Moreno-Chamarro et al., 2020). Moreover, the ITCZ in the Atlantic may also respond to bi-decadal and centennial patterns of change in Arctic sea ice (Liu & Fedorov, 2019), North Atlantic SST (Moreno-Chamarro et al., 2020), and AMOC strength (Vellinga & Wu, 2004), showing the complex nature of the ITCZ and the competing mechanisms that drive the position of atmospheric tropical convection. In Vellinga & Wu (2004), subtropical low-salinity anomalies generated as a result of the northward shift of the ITCZ are advected northward to the subpolar Atlantic within five to six decades, where they decrease the density and thus weaken the buoyancy-driven overturning.

Consistent with these two different types of atmospheric teleconnections (via mid-latitude Rossby waves and via equatorial waves, respectively), the AMOC response may follow two timescales - fast (decadal) and slow (multi-decadal to centennial), as a much longer time is needed for the oceanic salinity signal from the tropical Atlantic to propagate to high-latitudes and modify the AMOC. As the AMOC changes, it alters the North Atlantic climate through the transports of waters of different properties (temperature, salinity) and the response of the atmosphere to the changes.

Classically, the climate impacts of AMOC variations have been investigated through hosing experiments, where anomalous fresh water is artificially added or removed from the North Atlantic to modulate deep-water formation (e.g. Jackson 2015, 2018). Such an approach,

however, can introduce artificial changes in the subpolar area. As an example, added fresh water modifies upper-ocean stratification, which may affect sea ice and distort the AMOC effect on climate (discussed in Thomas & Fedorov (2019)). In addition, hosing experiments can misrepresent the mechanism transporting moisture from the Atlantic to the Pacific basin through central America (Liu et al., 2017). In a warming climate, this moisture transport may increase, imposing a negative feedback that would increase Atlantic sea surface salinity (SSS, Durack and Wijffels, 2010; Durack et al., 2012) and stabilize AMOC (Latif et al., 2000; Swingedouw et al, 2007; Richter and Xie, 2010). Forcing an AMOC change by teleconnections from the TIO allows us to investigate more robustly the impact of an amplified or dampened AMOC on the North Atlantic climate.

The experimental design of this study (next section) generally follows the approach of HF19, but the model used here (IPSL-CM6A-LR, Boucher et al. 2020) is a state-of-the-art coupled model with much higher both ocean and atmospheric model resolutions (e.g. nominal oceanic resolution 1º versus 3º in HF19). Furthermore, the current model has reduced SST and sea ice biases when compared to the CESM1 configuration in HF19, which was too cold and had a too large sea ice cover in the Arctic and Subarctic regions. The current model is correctly representing the location of major deep-water formation sites of the Labrador Sea and the interior of the Nordic Seas (Fig. 2). In contrast, the HF19 model had deep-water formation largely off the coast of Norway and the region south of Iceland, and no deep convection in the Labrador Sea. Therefore, the new experiments offer a more in-depth analysis of both the “fast” and “slow” responses of the TIO-North Atlantic teleconnection and, most importantly, allow us to conduct a thorough analysis of water mass transformation in the Labrador and Nordic seas responsible for the AMOC changes. Finally, examining the response of the AMOC to TIO warming with another coupled model allows us to confirm the robustness of the link between the Indian ocean temperature change and the North Atlantic.

One of the objectives of this analysis is to better quantify the timescales of AMOC variability and the sensitivity of AMOC and North Atlantic air-sea-ice interactions to the rTIO warming. This analysis introduces the rTIO-AMOC relationship within a coupled-model framework, with the indication to further use the results to explore interactions between AMOC and Arctic sea ice and the effect of mean AMOC changes on AMOC low-frequency variability.

The paper is organized as follows. Section 2 details the coupled model and the experiment setup. The results are presented and discussed in section 3, within four subsections, detailing initial anomalies, the fast response, slow response, and the rTIO-AMOC relationship respectively. The analysis of model water mass transformation in the North Atlantic is also included in this section. Finally, conclusions are in Section 4.

2. Model and Experimental Configuration

2.1 Model Configuration

This study is based on the coupled earth system model IPSL-CM6A-LR (IPSL-CM6 thereafter), recently developed at the IPSL (Institut Pierre-Simon Laplace) and participating in CMIP6. The model configuration is described in depth in Boucher et al. (2020) and the tuning procedure in Mignot et al. (in rev.). The coupled-model is composed of the atmospheric model LMDZ version 6A-LR (Hourdin, et al., 2019), the land-surface model ORCHIDEE version 2.0 (Krinner et al., 2011), and the oceanic model NEMO version 3.6 (Vancoppenolle et al., 2009; Aumont et al., 2015; Rousset et al., 2015; Madec et al., 2017).

The IPSL-CM6 has a regular atmospheric grid resolution with 144 longitude by 142 (latitude) grid points. In the vertical, the atmospheric model has 79 layers. The LMDZ model includes parameterizations of gravity waves, convection (Lott & Guez, 2013), and fronts (de la Cámara & Lott, 2015; de la Cámara et al., 2016). The ocean model NEMO includes three major components: the ocean physics (NEMO-OPA; Madec et al., 2017), the sea-ice dynamics

and thermodynamics (NEMO-LIM3; Vancoppenolle et al., 2009; Rousset et al., 2015), and the ocean biogeochemistry (NEMO-PISCES; Aumont et al., 2015). The eORCA1 ocean configuration that we used operates on a quasi-isotropic global tripolar grid; 1° nominal resolution and increases latitudinal resolution to 1/3° in the equatorial region. Vertically, the model utilizes a hybrid sigma-pressure coordinate, where the initial layer thicknesses increase non-uniformly. Layer thickness varies from 1 m at the surface, 10 m at 100 m depth, and 200 m in the bottom layers (75 vertical levels).

2.2 The Experimental Setup

To achieve an increased or decreased rTIO, a simple Newtonian relaxation (or nudging) of surface temperature is imposed at each timestep, using a long-term control run as the starting point. For each experiment, three ensemble members are launched from the same model-year of the 1100 years-long IPSL CM6A-LR piControl r1i2p1f1 (hereafter referred to as r1i2), allowing for a direct comparison of the ensemble members and the long-term control run. Note that r1i2p1f1 only differs from r1i1p1f1 from the computing machine, and this second member is preferred here as it uses exactly the same supercomputer as the one used for the sensitivity experiments of the present study. This simulation is marked by the same centennial variability as r1i1p1f1 (Boucher et al. 2020; Jiang et al., 2021). Variability is strongest in the Arctic and North Atlantic sector but also impacts the global mean sea surface temperature (not shown or ref). It is thought to be linked to the build-up of salinity anomalies within the Arctic, which subsequently leads to large fluctuations of deep convection within the Labrador and Nordic Seas (Jiang et al., 2021). Model-year 1950 of r1i2p1f1 is selected as an acceptable starting year as it is approximately between a peak and a trough of the centennial AMOC variability. All members were run for 100 years to compare the initial and transient response of the system as the TIO is nudged to a new state and the global climate reaches a new equilibrium. Selected

members were extended to 250 years to fully capture the new equilibrium and the potential influence on decadal and centennial variability within the IPSL-CM6. The TIO region nudged in the experiments is defined as 30°-100°E, 30°S-30°N (shown in Fig. 1). Several experiments are conducted wherein the TIO is continuously nudged towards monthly SST values of the r1i2 corresponding segment to which anomalies of +1°C, +2°C, -1°C, and -2°C are respectively added. A fixed surface restoring value of -40 W m^{-2} K^{-1} is applied, resulting in approximate mean SST changes in the TIO of +0.7°C, +1.4°C, -0.7°C, and -1.4°C from the control (rTIO changes of +0.3°C, +0.6°C, -0.3°C, and -0.7°C), respectively. HF19 reports that the TIO and rTIO have been steadily warming since the 1950s by 0.15°C and 0.05°C per decade, respectively, which is equivalent to an about +1ºC TIO and 0.3ºC rTIO anomaly that developed over the past 70 years. Thus, the magnitude of the imposed perturbation in the +1ºC nudging experiment compares well with observations of the last decades, even though imposed abruptly; other experiments serve to investigate the overall sensitivity of the climate system to TIO changes.

Also note that in applying the SST nudging and the surface restoring, the final change in SST is not exactly equal to the target value of nudging as some of the energy is distributed throughout the mixed layer and atmosphere, as well as by definition of a Newtonian relaxation the SSTs are nudged toward and not set to a value. Nevertheless, for simplicity, we will refer to these experiments as +1°C, +2°C, -1°C, and -2°C. To compare the variability and spread of the experiments, an additional ensemble of three control members is launched from the same initial r1i2 conditions, but are not nudged in the TIO like the three sensitivity experiments. This experimental setup is broadly similar to HF19 which used the National Center for Atmospheric Research's Community Earth System Model (CESM1) version 1.0.6, but here we apply a wider range of nudging and a weaker restoring coefficient.

Overall, at 26°N, IPSL-CM6 underestimates the AMOC (~13.5 Sv) by approximately 25% (~3.5 Sv) compared to the RAPID-MOCHA array (~17 Sv between 2004-2016; Smeed et al., 2018; Boucher et al. 2020). In this study, the AMOC strength is measured as the maximum overturning stream function from 500 to 2000m and between 44 and 45°N (referred to as 45°N), the approximate location of maximum overturning within the IPSL-CM6 model (Boucher et al., 2020), see Fig. 3a. Using 45ºN latitude in depth space has been done in other previous studies (i.e. Jackson et al., 2016; Ortega et al., 2017), although estimating AMOC further north would be ideal in density space due to possible compensation of water masses of different density flowing at similar depths. Therefore, to investigate the North Atlantic convective regions, the surface heat and freshwater fluxes are thoroughly investigated through a water mass transformation (WMT) analysis in density space (Walin, 1982; Speer and Tziperman, 1992; Speer et al., 2000). Further, the maximum overturning is broken into the Ekman and buoyancy-driven components. Meridional Ekman transport is estimated through the zonal wind stress at the air-sea interface. Both the AMOC strength and meridional Ekman transport are computed at 45°N. Similar to Ortega et al. (2015), we also define the buoyancy-driven components as the meridional overturning index (MOI) by removing the Ekman component at 45°N. Therefore, the MOI is defined as:

$$MOI = AMOC - Ekman_{merid.}$$

2.3 Deep Convective Regions and Water Mass Transformation

To identify the potential regions of deep-water formation in the North Atlantic that drive overturning within IPSL-CM6, we analyze winter (January - March) mean surface neutral density (γ_n) and mixed layer depth. Based on the North Atlantic density maxima co-located with the area of mixed layer depth variability exceeding 300m, similar to Escudier et al. (2013) and Ortega et al. (2015), we define Labrador (A) and Nordic Seas (B) as two key regions (Fig. 2). The boundary of each region is then selected based on bathymetric features. The Labrador

236 Sea region extends to the ridges along the Davis and Denmark Straits, is separated from the
237 eastern subpolar region by the Reykjavik Ridge, and extends to 48°N, the approximate AMOC
238 maximum. Therefore, our convective regions are defined based on a combination of
239 bathymetric features and ocean dynamics; first analyzing the mixed layer and density and then
240 separating the key regions based on bathymetry.

241 The eastern subpolar region from Iceland to Scotland was initially considered in the
242 analysis, but then removed due to the minimal impact of mean density and mixed layer depth
243 variability on AMOC within the IPSL-CM6 framework (Fig. 2 shows the minimal mixed layer
244 depth variability within the region). The subsequent water mass transformation analysis
245 confirmed that this region does not contribute to deep convection in this particular model. The
246 eastern subpolar region was undoubtedly important throughout previous IPSL coupled-models
247 (i.e. Mignot and Frankignoul, 2010; Msadek and Frankignoul, 2009; Escudier et al., 2013;
248 Ortega et al., 2015), but the Labrador and Nordic Seas have increased convection in the new
249 IPSL-CM6 (Boucher et al., 2020). Compared to the results of Escudier et al. (2013) and Estella-
250 Perez et al., (2020) using IPSL-CM5, there is increased surface density and mixed layer depth
251 variability in the Labrador Sea extending closer to the Davis Strait within IPSL-CM6 (Fig. 3).
252 Note that HF19 used CESM with the region south of Iceland being one of the two major deep
253 convection sites, but no convection in the Labrador Sea.

254 To understand the impacts of the fast versus slow TIO teleconnection, we thus analyze
255 WMT (Walin, 1982; Speer and Tziperman, 1992; Speer et al., 2000) and deep-water formation
256 within the Labrador and Nordic Seas regions. WMT is used as a diagnostic to attribute changes
257 in the ocean to surface heat and fresh water fluxes. To identify the role of diabatic processes in
258 WMT, monthly surface buoyancy-forcing is projected onto isopycnals between 22 and 29
259 sigma (sigma = density – 1000 kg m^{-3}). The buoyancy-forcing is binned by density classes of

0.05 kg m^{-3}, so as to precisely account for WMT into denser, deep-water formation within the convective areas.

Deep-water mass formation represents the volume convergence or divergence in density space. Traditionally, the Labrador Sea Water (LSW) is divided into two density classes, sigma of 27.68–27.74 kg m^{-3} and 27.74–27.80 kg m^{-3} (Kieke et al., 2006), but here it will be defined based on the densities and winter mixed layer depth variability of the control experiment as waters denser than sigma of 27.70 kg m^{-3}. In the Nordic Seas region, we will consider waters denser than sigma of 28.10 kg m^{-3} as another major source of North Atlantic Deep-Waters (NADW), since these densities are collocated with regions of maximum winter mixed layer depth variability in the control experiment (not shown). We therefore have separate criteria to represent deep water masses, based from the WMT and further discussed in section 3.3 of the *Results*.

3. Results

3.1 The impacts of TIO temperature change on the AMOC

We first investigate the AMOC response to the imposed TIO warming. For this, we first analyze the maximum overturning at 45°N and its two components - the wind-driven meridional Ekman transport and the buoyancy-driven overturning (given by MOI, defined in section 2.2). Ekman transport represents the high-frequency AMOC variability, while MOI the low-frequency variability. The mean AMOC at 45°N is approximately 11Sv ±1Sv (Fig. 3a & 4a) in the control run ensemble. Nudging the TIO generates a response in both AMOC and MOI within two-decades and influences the wind-driven Ekman transport within the first year of the experiment. In both the +1°C and +2°C TIO experiments, the AMOC diverges from the control ensemble after 15 years of nudging and exceeds the magnitude of control experiment with 95% confidence after 40 years (Fig. 4a, c; further discussed in section 3.2). Further

decomposition of AMOC details the rapid response in Ekman transport opposing the changes to the MOI: the MOI diverges from the control ensemble within 10-years, but this is not captured through AMOC alone, as the Ekman transport and MOI components initially compete.

Changes to the Ekman transport occur on an annual-scale: it shifts to a new mean state value as soon as the nudging is applied. The initial response in Ekman transport depends linearly on the nudging target, but also shows strong annual and decadal variability. The rTIO temperature has a clear influence on the subpolar westerlies and decreases the Ekman transport by -0.7 Sv in the +2°C (increases by +0.7 Sv in -2°C) experiment. This result illustrates the importance of this rTIO to global teleconnections in modeling and reanalyses (Liu et al., 2020). The MOI responds more gradually, its anomaly taking multiple decades to exceed the control experiment variability.

Within the initial 100-years of the experiments, the response to the rTIO dominates AMOC change, initially overshadowing decadal variability. Decadal variability begins to return to the control amplitude in the warming ensembles members only and after 50 to 70 years (see figure 4a and 4c). In the +2°C TIO members, the MOI reaches a new mean state after 150 years, displaying enhanced patterns of variability, including the centennial variability. The -2°C TIO member the AMOC declines until it is shut off and the circulation almost solely wind-driven. The latitude-depth composites of the approximate equilibrium of AMOC for the +2°C TIO (Fig. 3b) and -2°C TIO (Fig. 3c) show the enhanced overturning cell within the warming-TIO members and the net increased southward transport within the surface subpolar region of the cooling-TIO member. The +1°C and -1°C members lie in between these two extremes.

The MOI in Fig. 4c is used as a low-frequency variable to describe the three key phases in the ocean response. The initial response is defined as the first 10 years of the experiment.

The transient response occurs between years 11 and 30, chosen as the experiments begin to diverge from the control experiment but do not exceed the long-term variability (Fig. 4c). The near-equilibrium phase is reached in years 151 to 200. During that time, the ensemble mean of the +2°C experiment is within the respective long-term experiment 95% confidence interval. These near-equilibrium phase further corresponds to the time scale also identified in HF19. We now describe in more details these successive adjustments.

3.2 Initial Atmospheric Response and oceanic Transient Anomalies

As we increase the TIO SST in the +2°C experiment, a robust initial response develops (within a year, not shown) in sea level pressure (SLP) and SST over the North Atlantic (Fig. 1), including the formation of a positive NAO-like pattern: the North Atlantic subtropics exhibit increased SLP and SST, while the subpolar region displays decreased SLP and SST. A similar but opposite pattern emerges in the -2°C ensemble while here again the +1°C and -1°C responses show consistent and intermediate responses. Such generation of NAO-like patterns by TIO temperature anomalies has been previously modelled and observed (e.g. Bader and Latif, 2003; 2005; HF19; Baker et al., 2019) and shown to drive sea ice (Caian et al., 2018) and AMOC (Delworth and Zeng, 2016) variability on timescales longer than interannual. The observed warming in the TIO is furthermore thought to be contributing to the positive patterns observed in the NAO phase within the last several decades (Bader and Latif, 2003; 2005; Baker et al., 2019). The anomalous NAO-like patterns in SLP and corresponding wind changes (Fig. 5) drive anomalous SST (Fig. 1) and heat fluxes (Fig. 5) in the North Atlantic (e.g. Lee et al., 2011; Park et al., 2015).

In the tropical Atlantic of the +1°C and +2°C experiments, there is furthermore an anomalous SST dipole, with negative anomalies between 5°N-20°N and positive ones between 5°N-20°S (opposite signals for cooling TIO members, Fig. 1). This pattern relates to the

335 southward shift of the ITCZ (further described in section 3.4) and is important in forming the
336 tropical Atlantic sea surface salinity (SSS) anomalies (HF19; HF20, see section 3.4).

337 In the subsequent years, during the transient phase (years 11-30; Fig. 5), the responses
338 in the warming and cooling ensembles project aspects of spatially symmetric linear patterns
339 across the tropics and, in part, the North Atlantic. The atmospheric response over the North
340 Atlantic described above in turn drives anomalous surface density, heat fluxes, and wind stress
341 (Fig. 5) to the North Atlantic throughout the transient period (similar magnitude and spatial
342 results for years 11-20 or 11-40). In the warming TIO members (opposite for cooling TIO
343 members), there are positive surface density anomalies of 0.2 to 0.6 kg m^{-3} within the North
344 Atlantic convective regions; shown as the spatial patterns within the Labrador and Nordic Seas
345 and along the North Atlantic Current (Figs. 5b, c vs. Fig. 5a). Moreover, there is increased
346 zonal wind stress up to 50 x 10^{-3} N m^{-2} (Fig. 5e) and increased ocean to atmosphere heat fluxes
347 of 40 W m^{-2} along the sea ice extent in the Labrador and Nordic Seas and subpolar North
348 Atlantic (Fig. 5h) within the warming experiment. Net surface heat fluxes are reduced by 40
349 W m^{-2} (Fig. 5h) along the sea ice extent of the control run in the Nordic Seas and increase by -
350 40 W m^{-2} along the experiment sea ice extent in the subpolar North Atlantic. This finally
351 corresponds to a poleward shift of the heat fluxes as sea ice retreats. The opposite is found for
352 the cooling experiments. These three elements density, wind stress, and surface heat flux all
353 potentially contribute to enhanced deep convection in the northern North Atlantic in the
354 warming TIO members, and decrease it in the cooling ones.

355 These results generally agree with past analyses. Increased atmospheric convection
356 within the TIO was shown to increase the atmospheric sensible surface heat fluxes (from
357 increased poleward moisture fluxes) and reduce sea ice volume (extent and thickness) in the
358 North Atlantic and Arctic (Park et al., 2015). Such pattern results in the ocean exposed to
359 increased heat exchange with the atmosphere in the Nordic Seas and a poleward shift of the

subpolar jet (Lee et al., 2011). Olonscheck et al. (2019) further showed the importance of poleward atmospheric moisture transports, acting as a key driver modulating sea ice variability in observations, reanalyses, and models. In the study of Lee et al. (2011), the increased atmospheric convection throughout the TIO (related to TIO warming) resulted in a poleward shift of the upper tropospheric jet in the Atlantic subpolar region and induced anomalies similar to an NAO-like pattern. Similar mechanisms are discussed in HF19.

The expansion and contraction of sea ice resulting from the TIO teleconnection are important for the anomalies of surface density, heat flux, and wind stress (Bader and Latif, 2005; Lee et al., 2011; Park et al., 2015), but also to drive AMOC and surface anomalies that follow the pattern of an NAO-like climate response (Sévellec et al., 2017; Liu et al., 2019; Liu and Fedorov, 2019; HF19; Hu and Fedorov, 2020). A significant (two-sample t-test, 95% confidence level) asymmetry in the responses to the warming and cooling TIO experiments is observed in the response in sea ice. The mean (± 95% confidence interval) winter sea ice area of the control for the Labrador Sea is $18 \pm 3 \times 10^5$ km^2 and the Nordic Seas is $8.7 \pm 1.4 \times 10^5$ km^2. In the +2°C warming members, sea ice area decreases throughout the Labrador Sea by $4.8 \pm 1.5 \times 10^5$ km^2 in the ocean transient period (years 11-30; solid vs. dashed contour in Fig. 5h) and by $3.3 \pm 0.5 \times 10^5$ km^2 within the Nordic Seas. In both the Labrador and Nordic Seas basins, the increased rTIO thus results in a significant decrease in sea ice area. However, in the cooling members (Fig. 5i), sea ice area is statistically similar to the control run in the Labrador Sea and there is an expansion of sea ice area in years 11-30 by $2.2 \pm 0.6 \times 10^5$ km^2 (-1°C experiment) and $4.5 \pm 1 \times 10^5$ km^2 (-2°C experiment; Fig. 5i) within the Nordic Seas for the same transient period.

3.3 AMOC "Fast" Response: Deep Convection and Water Mass Transformation

Now that we have shown that a quasi-instantaneous response settles, we show how it impacts AMOC via modifying deep water formation. Using sensitivity experiments, Garcia-Quintana et al. (2019) show that anomalous North Atlantic heat fluxes driven through the TIO teleconnection are an important driver of the Labrador Sea dense water formation. WMT is used to measure the role surface buoyancy-forcings and diabatic processes in the North Atlantic dense water formation. The total WMT (Fig. 6) is separated into its additive surface heat and fresh water flux contributions. Both modify the surface density, and hence the WMT rates (Speer et al. 2000). In the Labrador Sea and in the control simulation, heat loss to the atmosphere acts to transform water masses to higher densities, with a peak of ~12 Sv near a sigma of 28 (Fig. 6). Conversely, in this precipitation and sea-ice melting region, fresh water flux acts to transform waters to lighter density, but not enough to offset the transformation by heat fluxes. A similar balance occurs for the Nordic Seas, albeit with a broader density range for heat flux driven transformation and a stronger impact of sea-ice melting above 28. To quantify the net effect of transformation per density class, the divergence of WMT (referred to as formation rate) is used to relate the oceanic response in the North Atlantic to the TIO anomalous warming or cooling.

Within the Labrador Sea, the total formation of dense water shifts to higher density waters for the warming rTIO members (Fig. 7a) and significantly increases in magnitude. In the +2°C TIO members, approximately 3 Sv of waters denser than 28 are formed additionally when compared to the control experiment (Fig. 7a). Opposingly, formation in the -2°C TIO members shift towards less dense waters: 3sv of water lighter than 28 are formed as compared to the control (Fig. 7a). Changes in the surface heat flux (Fig. 7b) drive the changes in magnitude of deep-water formation in both the warming and cooling experiments.

The fresh water flux (Fig. 7c) on the other hand has a significant, but small, contribution to forming less dense waters only. HF19 note the increased heat fluxes throughout the Labrador

409 Sea in response to the TIO warming, but notably their model does not show deep convection
410 in this region. Here, we show that these increased surface heat fluxes (Fig. 7b) result in changes
411 to the Labrador Sea. These results are partly consistent with the sensitivity experiment of
412 Garcia-Quintana et al. (2019), noting that, in their model, the surface fresh water flux does not
413 significantly change the Labrador Sea dense water formation, but changes are rather heat fluxes
414 driven. In our experiment, the surface fresh water flux contribution to dense water formation
415 is significant in the warming experiments (waters denser than 27.7; section 2.3), but it is lower
416 in magnitude and compensates the changes driven by the surface heat fluxes.

417 Anomalies in the Nordic Seas dense water total formation rates (Fig. 7d; denser than
418 28.1) are driven through both heat and fresh water flux contributions. At a density near γ_n of
419 28.3, there is an increase in magnitude in the warming experiments. In the +2°C TIO
420 experiment, the surface heat flux (Fig. 7e) drives an increase of 3 Sv of waters denser than 28.3
421 and the surface fresh water flux (Fig. 7f) drives the shift in formation of waters near 28.2 to
422 create approximately 2 Sv of waters between 28.0 and 28.1. In the -2°C members, the surface
423 fresh water flux significantly contributes to the formation of less dense waters and increases
424 the formation of waters between 27.9 and 28.1 by 2 Sv. There are similar results for the +1°C
425 and -1°C experiments, but lower magnitudes of formation rates than the +2°C and -2°C
426 experiments respectively. This analysis depicts an increase of dense water formation in the
427 warming experiments and a shift to less dense waters in the cooling experiments in the Nordic
428 Seas in response to the TIO teleconnection.

429 As seen in Fig. 5, the Nordic Seas respond to the warming rTIO with a significant
430 decline of sea ice on top of the increased surface density. The opposite is true for the cooling
431 rTIO. A similar relationship was shown by Park et al. (2015): as the atmospheric convection
432 increases throughout the TIO (the key mechanism in driving this teleconnection from HF19),
433 the amount of atmospheric moisture transported poleward into the Arctic increases, resulting

434 in increased downward surface heat fluxes into the Arctic. Simultaneously, as the downward
435 heat flux increases, there is a resulting retreat of sea ice within the Nordic Sea. Moreover, the
436 enhanced TIO convection results in the poleward shift of the subpolar westerlies (Lee et al.,
437 2011), which can contribute to the reduction of sea ice and the vertical mixing throughout the
438 water column. Although a more detailed analysis would be needed to verify these mechanisms
439 in the present model, in the warming experiments, where the westerlies have intensified and
440 where there in a retreat of sea ice within the Nordic Seas, the shift in the westerlies allows for
441 the distinct boundary of heat and fresh water flux anomalies to be mixed along isopycnals. The
442 opposite is true for a cooling TIO and finally, both heat and freshwater components contribute
443 to the total formation rates of dense waters within this region.

444 Time-series of anomalous dense water formation in the Labrador Sea ($\gamma_n \geq 27.7$) and
445 Nordic Seas ($\gamma_n \geq 28.1$) from the respective convective regions are shown in Fig. 8. The
446 anomalous formation in the Labrador Sea of the +2°C TIO experiment begins to separate from
447 the control experiment spread within the first 10 years, exceeding the 95% confidence interval
448 of the control experiment by year 30. Nearly twice as long is needed in the +1°C experiment
449 as a result of the strong multi-decadal variability and the weaker forced signal. The mean
450 anomaly for the Labrador Sea formation in the +2°C experiment for the ocean transient period
451 (years 11-30) is 2.6 ± 0.6 Sv and the near-equilibrium phase (years 151-200) is 9.3 ± 1.3 Sv.
452 The -1°C TIO experiment results in a decrease of -1.7 ± 0.6 Sv during the ocean transient phase
453 and of -1.8 ± 0.5 Sv in the near-equilibrium. Changes in both warming experiments are
454 significant at the 95% confidence interval in the near-equilibrium timescale. The warming
455 experiments show increased magnitude of net formation, but also increased multi-decadal
456 variability after the year 30, while decreasing variability in the -1°C experiment. In the -2°C
457 TIO members, the Labrador Sea deep-water formation anomaly is not significant for the
458 transient phase.

In contrast, the Nordic Seas deep-water formation exceeds the control ensemble spread several decades after that of the Labrador Sea (Fig. 8b), with the timescales depending on the magnitude of the TIO experiment. The +2°C TIO members separate from the control roughly 30 years into the experiment, while the +1°C TIO members lag by more than 80 years. The anomalies in all experiments are not significant during the transient phase of years 11-30. The mean deep-water formation anomaly in the Nordic Seas for the +2°C experiment in the near-equilibrium phase is +6.7 ± 0.4 Sv. The cooling experiments show a bi-decadal pattern of variability until the Nordic Seas region begins to be covered with ice and the change in fluxes induce the shift in formation. Ultimately, near year 110, the negative anomaly of dense water formation in the Nordic Seas is in a reduced state as sea-ice prevents exchanges of surface heat and freshwater fluxes and the formation of dense waters at the surface. In the warming experiments, the initial 100 years of the experiments display increased multi-decadal variability, which is stabilized in the Nordic Seas in the +2°C experiment by year 100 and amplifies in magnitude in the Labrador Sea.

To conclude, the WMT and changes in deep-water formation rates quantify the shift of density classes within the Labrador and Nordic Seas. The fast response from the TIO teleconnection results in the significant change to the formation of dense water in the Labrador Sea, largely driven through the surface heat fluxes. The Nordic Seas dense water is created through the surface heat fluxes for the warming members and is reduced by changes in the fresh water flux for the cooling ones; although the Nordic Seas dense water formation anomalies do not exceed the 95% confidence interval of the control experiment before several decades. The results indicate the ocean transient response to the warming rTIO is primarily due to the creation of dense waters in the Labrador Sea, largely attributed to the increased heat flux over the convective region, while significant changes to Nordic Seas dense water formation occur after the transient period.

3.4 "Slow" Response: Tropical Atlantic Salinity Anomalies and the salt-advection feedback

We now describe qualitatively the slow mechanism inducing the change in AMOC mean state and variability. Figure 9 illustrates the spatial evolution of precipitation, sea surface salinity (SSS), and SST anomalies throughout the +2°C experiment (opposite sign, but similar spatial patterns in the -2°C experiment) throughout the whole Atlantic. Within the first five years of the experiment (cf. section 3.2), there is a significant decrease in the tropical Atlantic precipitation (approximately 10°N to 20°S). This response is consistent with the strengthening of the Atlantic Walker circulation and increased subsidence demonstrated in HF19. In the transient period (years 11-30) the precipitation significantly decreases by -0.27 ± 0.3 mm day^{-1} and salinity increases by 0.5 ± 0.1 g kg^{-1} in the eastern tropical Atlantic (10°N-20°S, 20°E-20°W), while there is a net increase in precipitation of 0.32 ± 0.5 mm day^{-1} (not significant) at approximately 10°N in the tropical Atlantic.

The spatial change in annual precipitation illustrates the Hadley cell (meridional) response to the anomalous Walker circulation (zonal response) resulting from the TIO warming: a northward shift of the ITCZ and a decrease in precipitation throughout the southern tropical Atlantic basin for years 11-30. The atmospheric response in the tropical Atlantic relates to the meridional Hadley circulation, which is thought to narrow and increase precipitation under a climate warming scenario (Gastineau et al., 2008; Byrne et al., 2018; Watt-Meyer et al., 2019), although not addressing the impacts of a weakening AMOC or warming rTIO in the climate scenarios. The narrowing of the Hadley cell and enhanced Walker circulation (not shown here) results in the increased SSS throughout the tropical Atlantic via a combination of the increased winds (Fig. 5c,d; contributing to evaporation) and decreased precipitation along the equator (HF19). Additionally, there are precipitation changes over continental South America and Africa in the IPSL-CM6 experiment, which such anomaly can influence the

509 tropical stability and freshwater discharge of major rivers along the coasts (Grodsky et al.,
510 2014).

511 Note that after the first several decades, the precipitation anomalies and the location of
512 the ITCZ are probably driven through both the TIO mechanism on tropical stability and also
513 the adjustment to AMOC strength from the fast atmospheric response. An enhanced AMOC
514 indeed tends to be associated with an anomalously warm northern tropical Atlantic ocean and
515 thus a northward shift of the ITCZ (Vellinga & Wu, 2004; HF19; Moreno-Chamarro, 2020).
516 This effect on AMOC can then influence the rate of northward advection and the magnitude of
517 salinity anomalies in the tropical Atlantic.

518 The SSS anomalies produced in the tropical Atlantic represent the starting point of the
519 slow response described in Hu and Fedorov (2020) to TIO nudging. These anomalies can act
520 as a mechanism to drive AMOC variability, as the anomalies circulate around the subpolar gyre
521 and the North Atlantic drift, reaching the deep convection regions and modifying the deep
522 water formation, thereby AMOC. A similar mechanism of tropical Atlantic salinity anomalies
523 was originally described in Vellinga & Wu (2004), and later by Mignot & Frankignoul (2010),
524 Menary et al. (2011), and Jackson & Vellinga (2013), investigating the relationship between
525 AMOC variability and the advection of salinity anomalies from the tropical Atlantic to the
526 subpolar region.

527 In our experiment, SSS anomalies are present in the Caribbean and Florida Currents
528 within the first five years of the experiments, collocated with precipitation anomalies (Fig. 9).
529 These anomalies are expected to be advected northward towards the northern North Atlantic
530 by the mean circulation after recirculation within the subtropical gyre, as discussed in several
531 previous study (e.g. Vellinga & Wu, 2004; Goelzer et al., 2006, Mignot et al., 2007). The
532 typical timescale ranges from three to four decades (Goelzer et al., 2006, Mignot et al., 2007)
533 to five to six decades in Vellinga & Wu (2004).

Fig. 9 further depicts the strong circulation of salinity anomalies in the +2°C TIO experiment: after several decades, salinity anomalies are recirculated within the Northern Hemisphere subtropical gyre. At longer timescale (years 71-100 and 151-200 from Fig. 9), both the extension of positive salinity and temperature anomalies along the eastern subtropical Atlantic and reduced positive salinity anomalies (compared to years 1-5 and 11-30) within the tropical Atlantic are signs of a strengthened AMOC (Fig. 9 middle right panels, and Zhang 2008; Zhang & Zhang, 2015; Jackson & Wood, 2020). The opposite pattern develops in the -2°C TIO members, albeit at a slower timescale, indicating a reduced AMOC (not shown).

Note that significant positive temperature and salinity anomalies are also present within the North Atlantic convective regions and Gulf Stream Extension by years 11-30 (Fig. 9), which is probably earlier than the advective process of salt transport from the tropical Atlantic. These positive SST and SSS anomalies during the years 1-5 and 11-30 result from the fast adjustment process described above.

For years 71-100 and 151-200, temperature and salinity anomalies in the subpolar North Atlantic are then driven through two key mechanisms: 1) The enhanced atmospheric heat exchange with the ocean and wind stress 2) Advective transports of salinity and heat in response to the AMOC strength. The response of SST (Fig. 9 i-l) further depicts the preferential warming of the subpolar North Atlantic compared to the tropics. There is an initial cooling response (years 1-5) within the subpolar region, under the competition effect of sea ice retreat and the NAO-like pattern. After the initial five years the pattern develops into continuous atmospheric warming and positive SST anomalies in the subpolar North Atlantic and Arctic. However, long-term variability of Atlantic SST in the tropics, subtropics, and subpolar regions have all been shown to co-vary with AMOC (Zhang 2008; Zhang & Zhang, 2015; Jackson & Wood, 2020) and the Atlantic multidecadal variability (Biastoch, 2015).

To further illustrate the slow mechanism of salinity anomalies from the tropical Atlantic driving changes to the convective regions, Fig. 10 shows the propagation of salinity, potential temperature (theta), and density anomalies at 1700-2000 m depth for the +2°C and -2°C experiments. The first significant signal to develop in the +2°C experiment is from temperature. There are significant negative temperature anomalies of magnitude -0.2°C originating between 55°-60°N, the approximate location of the subpolar convective regions, and propagating southward, reaching the Equator after ~70 years. This change in deep-water temperature occurs between years 11-20 and is collocated with an increase in density. However, by years 21-30 (and after), the deep-water becomes significantly both saltier and warmer, originating from the latitudes of the North Atlantic convective site (55°-75°N). The temperature and salinity anomalies continue to increase after the ocean transient phase (years 11-30), as salinity anomalies become stable near 0.3 g kg^{-1} and temperature anomalies reach 1.6°C by year 120, thereafter varying as a result of AMOC variability (Zhang 2008; Zhang & Zhang, 2015). A different signal develops in the -2°C (not symmetric with the +2°C), where there is no signal north of 60°N in the subpolar North Atlantic, a slower adjustment to equilibrium, and lower variability.

These Hovmöller diagrams indicate that the temperature anomalies drive the density signal in the high latitudes within the first 20 years of the experiment, while after 30 years the signal is driven through salinity anomalies. This change in the driver of deep-water formation anomalies demonstrates in our view the respective roles of the fast and slow mechanisms. As seen above, the fast response drives significant surface heat fluxes anomalies, which result in increased dense waters in the Labrador Sea and negative temperature anomalies at depth. When salinity dominates the density field, this testifies that the slow signal has reached the North Atlantic. The delay computed from the Hovmöller diagrams for increased salinity and temperature anomalies to arrive in the North Atlantic deep-water (roughly 30 years) generally

583 agrees with previous literature, yet with a modulation due to the fast response: this delay is
584 three to four decades in the +2°C experiment, due to the already enhanced AMOC, while it is
585 closer to four decades in the -2°C experiment, due to the already reduced AMOC.

586 The relative importance of the salt-advection feedback in the gradual strengthening of
587 AMOC versus the effect of initial salinity anomalies generated in the tropical Atlantic and then
588 advected to the north is difficult to quantify. The slow response is known to work on
589 multidecadal timescales, as anomalies from the tropical Atlantic take up to four decades to
590 reach the North Atlantic from the equatorial and tropical regions (Vellinga & Wu, 2004;
591 Goelzer et al., 2006, Mignot et al., 2007). The fast response of the teleconnection is shown to
592 interact on annual and decadal times-scales. Although, the differing timescales make it
593 challenging to separate the magnitude of AMOC response from the slow mechanism, the
594 response from the TIO drives strong changes to patterns of precipitation and salinity within the
595 first year of the experiments.

596

597 **4. Discussion and Conclusions**

598 Tentative evidence suggests the AMOC might have been in a state of decline or reduced
599 circulation throughout the past century (Caesar et al., 2021), and climate models suggest further
600 slow-down in the future (e.g. Liu et al. 2020). To that end, it is important to understand which
601 factors may affect the rate of current and future AMOC decline, or lack thereof. Here, we
602 investigate the effect of the relative warming or cooling of the Tropical Indian Ocean (TIO) on
603 the AMOC and detail two mechanisms that can drive AMOC changes on “fast” and “slow”
604 timescales. The response to the warming is especially important in the context of anthropogenic
605 climate change as the Indian ocean has been warming faster the rest of the tropical oceans (i.e.
606 Ihara et al., 2008; Rao et al., 2012; Roxy et al., 2014; HF19). Both mechanisms rely on
607 atmospheric teleconnections, but the fast mechanism drives changes directly in the subpolar

North Atlantic while the slow one acts through the tropical Atlantic Ocean and is communicated to the north by multi-decadal oceanic pathways. At quasi-equilibrium, we achieve an increase in AMOC of about 5 Sv in the +2°C-TIO, 3 Sv in the +1°C-TIO and a reduction of 3-4 Sv in the -1°C-TIO. The AMOC decreases by nearly 8 Sv in the equilibrium of the -2°C-TIO experiment, ultimately leading to the shutdown of the AMOC (Fig. 3c, 4c, 11c).

The AMOC is decomposed into the meridional Ekman transport and buoyancy-driven components (MOI). The Ekman transport changes within the first year of the perturbation experiments, as the TIO teleconnection directly influences the subpolar westerly winds. The MOI diverges from the control run approximately after a decade of the experiments. However, since the Ekman transport partially compensates the MOI response, the AMOC intensity starts diverging from the control only after 15-years (in the +2°C experiment). The fastest response occurs for the warming TIO experiments, but the largest magnitude change in the near-equilibrium AMOC occurs for the -2°C TIO members.

Analyzing the AMOC response to the rTIO we find (Fig. 11) a robust linear dependence across different experiments. The rTIO elicits a 7.0 Sv per 1°C response in the transient period and 9.4 Sv per 1°C at the approximate equilibrium (nearly 70% of the mean AMOC of the control r1i2), with a coefficient of determination (r^2) of 0.95 and 0.96 respectively, and both significant at the 95% confidence level. This implies that the imposed changes in TIO relative temperature explain 96% of the AMOC response in these experiments, signifying the potential importance of this rTIO-AMOC teleconnection and the rTIO temperature to modeling and understanding AMOC variability. Note that in the experiment of HF19, the response of AMOC to the rTIO was about 11.2 Sv per 1°C for years 151-200, although the mean AMOC in the NCAR CESM model used is closer to 17 Sv, roughly 25% stronger than the AMOC in the IPSL-CM6 piControl. Despite the mean AMOC value being stronger in their experiment, the

633 11.2 Sv per 1°C response is approximately 66% of the mean AMOC (17 Sv) and a very similar
634 ratio to this experiment.

635 In response to (warm) TIO anomalies, a fast atmospheric teleconnection from the Indian
636 basin to the North Atlantic first develops as a (positive) NAO-like pattern, which strengthens
637 subpolar westerlies and wind stress within the Labrador and Nordic Seas, the key deep-
638 convective regions within the North Atlantic. This NAO-like pattern also induces anomalous
639 atmospheric temperatures over to the Arctic region (not described in text), decreasing sea ice
640 over both convective sites. The resulting changes to the Ekman transport and surface fluxes
641 lead to increased deep-water formation in these two regions. Within the Labrador Sea, changes
642 in surface heat fluxes are the key mechanism in buoyancy-forcing, driving 3 Sv of additional
643 deep-water formation, while both the surface heat and fresh water fluxes are important to
644 increase deep-water formations by 2-3 Sv in the Nordic Seas. The fast rTIO-AMOC
645 relationship is thus driven through seasonal-scale atmospheric teleconnections, influencing the
646 deep-water formation during the first 10 years of the experiment. At this stage, the buoyancy
647 driven strengthening of the AMOC drives temperature anomalies at depth.

648 The slow adjustment process that follows results from a combination of both
649 atmospheric teleconnections and the Atlantic ocean northward advection and continues for the
650 duration of the simulations. Patterns of anomalous precipitation form within the first year of
651 the experiments in the subtropical Atlantic, and the resulting salinity anomalies reach the
652 northern regions of deep convection after 30 to 40 years (Fig. 10), consistent with the
653 multidecadal advective timescales shown by previous studies (Vellinga & Wu, 2004; Goelzer
654 et al., 2006, Mignot et al., 2007). While anomalous salinity is present throughout the Caribbean,
655 Gulf Stream, and North Atlantic Current within the initial 30 years, it is the fast response that
656 drives AMOC anomalies during these years. Anomalous salinity and temperature at 1700-2000
657 m depth indicate that density anomalies initially due to changes in temperature respond to

658 increased salinity after 30 years. The shift to salinity dominating the density signal signs the
659 influence of the ‘slow” response. It is concomitant with increased temperature anomaly,
660 characteristic of the waters advected from the tropical Atlantic. The salinity signal is possibly
661 further amplified by the salt-advection feedback.

662 It is also important to note that increasing the rTIO temperature in our model runs
663 results in increased variability in AMOC; the largest variability is in the +2°C experiment and
664 the least in the -1°C and -2ºC TIO simulations. This brings about an intriguing question of the
665 dependence of AMOC variability on the mean state of the AMOC and the North Atlantic, to
666 be investigated in a subsequent study.

667 Another new result of this study is that in the -2°C experiment there is a collapse of
668 AMOC at the end of the simulation, which occurs at rTIO=-0.7ºC. This finding provides an
669 alternative, tropical mechanism for abrupt climate changes seen in the paleo records of the
670 North Atlantic climate (see reviews in Rahmstorf 2002; Alley et al. 2003; Seager and Battisti
671 2007; or Clement and Peterson 2008) and typically associated with the reduction or collapse
672 of AMOC. A vast majority of theories explaining those AMOC changes rely on local fresh
673 water forcing in the high-latitude North Atlantic as the driver. The likelihood of this alternative
674 mechanism remains to be assessed in paleo data.

675 The collapse of the AMOC for strong negative TIO forcing is one of the asymmetries
676 we find in the response to cold versus warm TIO anomalies. Another asymmetry is that the
677 weakening of AMOC is driven largely through the Nordic Seas, while the strengthening is due
678 to changes in both the Labrador and the Nordic Seas, with changes in the former slightly larger
679 than in the latter,

680 To conclude, our results confirm that under anthropogenic global warming the
681 enhanced warming of TIO could act as a mechanism to stabilize AMOC, reducing the
682 magnitude of, or potentially delaying AMOC decline under the current and various climate

scenarios. The warming of TIO also sustains a positive NAO-like mean pattern affecting sea ice and the AMOC. However, should this enhanced relative warming of TIO no longer continue, one could expect a faster future decline of the AMOC. Conversely, should rTIO increase, the AMOC decline could be halted or even reversed.

To put these results into context, HF19 estimate that the TIO and rTIO are increasing by 0.15 and 0.05 °C per decade since the 1950s, respectively, which is equivalent to about +1ºC TIO and 0.3ºC rTIO warming. Therefore, both warming experiments are realistic in terms of the magnitude of the simulated TIO warming (+0.7 and 1.4ºC) but "extreme" in terms of the rate of the warming. Nevertheless, the TIO and rTIO temperature increases are two robust features linked to anthropogenic warming (Ihara et al., 2008; Rao et al., 2012; Roxy et al) interannual (fast) and multidecadal (slow) timescales. While the rate of TIO warming may be important for the details of the fast response, it should not matter for the eventual AMOC changes. Additionally, we advocate that bias in modelled rTIO SST could potentially lead to model biases in the AMOC mean-state values, as the relative SST gradient in tropics prove here to be an important teleconnection in driving AMOC. Future analyses decomposing and addressing AMOC variability should further be done to improve the understanding of the climate system and large-scale interactions and climate model projections.

Acknowledgements

This research is supported by the ARCHANGE project of the "Make our planet great again" program (ANR-18-MPGA-0001, France). Additional support is provided to AVF by NSF (OCE-1756682, OPP-1741841). JM is supported by the EUCP project funded by the European Union's Horizon 2020 programme (grant agreement number 776613). EG is also supported by Centre National de la Recherche Scientifique (CNRS). This work used the HPC resources of TGCC under the allocations 2019-A0070107403 provided by GENCI (Grand

Equipement National de Calcul Intensif) and we acknowledge PRACE for awarding us access to JOLIOT CURIE at GENCI@CEA, France. This study benefited from the ESPRI (Ensemble de Services Pour la Recherche l'IPSL) computing and data centre (https://mesocentre.ipsl.fr) which is supported by CNRS, Sorbonne University, Ecole Polytechnique and CNES and through national and international grants. The authors are grateful to Leonard F. Borchert, Didier Swingedouw, and Julie Deshayes for the thoughtful discussions on the methods and the manuscript.

References

Alley, R. B., Marotzke, J., Nordhaus, W. D., Overpeck, J. T., Peteet, D. M., Pielke, R. A., ... & Wallace, J. M. (2003). Abrupt climate change. *science*, *299*(5615), 2005-2010, doi:10.1126/science.1081056.

Aumont, O., Ethé, C., Tagliabue, A., Bopp, L., & Gehlen, M. (2015). PISCES-v2: an ocean biogeochemical model for carbon and ecosystem studies. *Geophys. Mod. Dev*., 8, 2465-2513, doi:10.5194/gmd-8-2465-2015.

Bader, J., & Latif, M. (2003). The impact of decadal-scale Indian Ocean sea surface temperature anomalies on Sahelian rainfall and the North Atlantic Oscillation. *Geophysical Research Letters*, *30*(22),doi:10.1029/2003GL018426.

Bader, J., & Latif, M. (2005). North Atlantic Oscillation response to anomalous Indian Ocean SST in a coupled GCM. *Journal of Climate*, 18(24), 5382-5389, doi:10.1175/JCLI3577.1.

Baker, H. S., Woollings, T., Forest, C. E., & Allen, M. R. (2019). The linear sensitivity of the North Atlantic Oscillation and eddy-driven jet to SSTs. *Journal of Climate*, *32*(19), 6491-6511, doi:10.1175/JCLI-D-19-0038.1.

Barnier, B., Madec, G., Pendu_, T., Molines, J.-M., Treguier, A.-M., Le Sommer, J., . . . De Cuevas, B. (2006). Impact of partial steps and momentum advection schemes in a global ocean circulation model at eddy-permitting resolution. *Ocean Dynamics*, 56, 543-567. doi:10.1007/s10236-006-0082-1.

Biastoch, A., Durgadoo, J. V., Morrison, A. K., Van Sebille, E., Weijer, W., & Griffies, S. M. (2015). Atlantic multi-decadal oscillation covaries with Agulhas leakage. *Nature Communications*, *6*(1), 1-7, doi:10.1038/ncomms10082.

Boucher, O., Servonnat, J., Albright, A.L., Aumont, O., Balkanski, Y.,. . . . Vuichard, N. (2020). Presentation and evaluation of the IPSL-CM6A-LR climate model. *J. Adv. Model. Earth Syst*, doi:10.1029/2019MS002010.

Buckley, M. W., and Marshall, J. (2016). Observations, inferences, and mechanisms of the Atlantic Meridional Overturning Circulation: A review. *Reviews of Geophysics*, 54(1), 5-63, doi:10.1002/2015RG000493.

Byrne, M. P., Pendergrass, A. G., Rapp, A. D., & Wodzicki, K. R. (2018). Response of the intertropical convergence zone to climate change: Location, width, and strength. *Current climate change reports*, 4(4), 355-370, doi:10.1007/s40641-018-0110-5.

Caesar, L., McCarthy, G. D., Thornalley, D. J. R., Cahill, N., & Rahmstorf, S. (2021). Current Atlantic Meridional Overturning Circulation weakest in last millennium. *Nature Geoscience,* 1-3, doi:10.1038/s41561-021-00699-z.

751 Caian, M., Koenigk, T., Döscher, R., & Devasthale, A. (2018). An interannual link between
752 Arctic sea-ice cover and the North Atlantic Oscillation. *Climate dynamics*, *50*(1), 423-
753 441, doi:10.1007/s00382-017-3618-9.
754 Cheng, W., Chiang, J. C., & Zhang, D. (2013). Atlantic meridional overturning circulation
755 (AMOC) in CMIP5 models: RCP and historical simulations. *Journal of Climate*,
756 26(18), 7187-7197, doi:10.1175/JCLI-D-12-00496.1.
757 Clement, A. C., & Peterson, L. C. (2008). Mechanisms of abrupt climate change of the last
758 glacial period. *Reviews of Geophysics*, *46*(4), doi:10.1029/2006RG000204.
759 de la Cámara, A., & Lott, F. (2015). A stochastic parameterization of the gravity waves emitted
760 by fronts and jets. *Geophys. Res. Lett.,* 42, 2071-2078, doi:10.1002/GL063298.
761 de la Cámara, A., Lott, F., & Abalos, M. (2016). Climatology of the middle atmosphere in
762 LMDz: Impact of source-related parameterizations of gravity wave drag. *J. Adv.*
763 *Modeling Earth Systems*, 8 (4), 1507-1525, doi:10.1002/2016MS000753.
764 Delworth, T. L., & Zeng, F. (2016). The impact of the North Atlantic Oscillation on climate
765 through its influence on the Atlantic meridional overturning circulation. *Journal of*
766 *Climate*, *29*(3), 941-962, doi:10.1175/JCLI-D-15-0396.1
767 Dong, L., & Zhou, T. (2014). The Indian Ocean sea surface temperature warming simulated by
768 CMIP5 models during the twentieth century: Competing forcing roles of GHGs and
769 anthropogenic aerosols. *Journal of Climate*, 27(9), 3348-3362, doi:10.1175/JCLI-D-
770 13-00396.1.
771 Du, Y., & Xie, S. P. (2008). Role of atmospheric adjustments in the tropical Indian Ocean
772 warming during the 20th century in climate models. *Geophysical Research Letters*,
773 35(8), doi:10.1029/2008GL033631.
774 Durack, P. J., & Wijffels, S. E. (2010). Fifty-year trends in global ocean salinities and their
775 relationship to broad-scale warming. *Journal of Climate*, 23(16), 4342-4362,
776 doi:10.1175/2010JCLI3377.1.
777 Durack, P. J., Wijffels, S. E., & Matear, R. J. (2012). Ocean salinities reveal strong global water
778 cycle intensification during 1950 to 2000. *Science*, 336(6080), 455-458, doi:
779 10.1126/science.1212222.
780 Estella-Perez, V., Mignot, J., Guilyardi, E., Swingedouw, D., & Reverdin, G. (2020). Advances
781 in reconstructing the AMOC using sea surface observations of salinity. *Climate*
782 *Dynamics*, 1-18, doi:10.1007/s00382-020-05304-4.
783 Escudier, R., Mignot, J., & Swingedouw, D. (2013). A 20-year coupled ocean-sea ice-
784 atmosphere variability mode in the North Atlantic in an AOGCM. Climate dynamics,
785 40(3-4), 619-636, doi:10.1007/s00382-012-1402-4.
786 Frierson, D. M. W., Hwang, Y.-T., Fučkar, N. S., Seager, R., Kang, S. M., Donohoe, A., et al.
787 (2013). Contribution of ocean overturning circulation to tropical rainfall peak in the
788 Northern Hemisphere. *Nature Geoscience*, 6(11), 940–944, doi:10.1038/ngeo1987.
789 Gastineau, G., Treut, H. L., & Li, L. (2008). Hadley circulation changes under global warming
790 conditions indicated by coupled climate models. *Tellus A: Dynamic Meteorology and*
791 *Oceanography*, 60(5), 863-884, doi:10.1111/j.1600-0870.2008.00344.x.
792 Garcia-Quintana, Y., Courtois, P., Hu, X., Pennelly, C., Kieke, D., & Myers, P. G. (2019).
793 Sensitivity of Labrador Sea Water formation to changes in model resolution,
794 atmospheric forcing, and fresh water input. *Journal of Geophysical Research: Oceans*,
795 124(3), 2126-2152, doi:10.1029/2018JC014459.
796 Goelzer, H., Mignot, J., Levermann, A., & Rahmstorf, S. (2006). Tropical versus high latitude
797 fresh water influence on the Atlantic circulation. *Climate dynamics*, 27(7-8), 715-725,
798 doi: 10.1007/s00382-006-0161-5.

Grodsky, S.A., Carton, J.A., Bryan, F.O. (2014). A curious local surface salinity maximum in the northwestern tropical Atlantic. *Journal of Geophysical Research: Oceans*, 119, 1-12, doi:10.1002/2013JC009450.

Heuzé, C. (2017). North Atlantic deep water formation and AMOC in CMIP5 models. Ocean *Science*, 13(4), 609, doi:10.5194/os-13-609-2017.

Hoerling, M. P., Hurrell, J. W., & Xu, T. (2001). Tropical origins for recent North Atlantic climate change. *Science*, 292(5514), 90-92, doi:10.1126/science.1058582.

Hoerling, M. P., Hurrell, J. W., Xu, T., Bates, G. T., & Phillips, A. S. (2004). Twentieth-century North Atlantic climate change. Part II: Understanding the effect of Indian Ocean warming. *Climate Dynamics*, 23(3-4), 391-405, doi:10.1007/s00382-004-0433-x.

Hourdin, F., Rio, C., Grandpeix, J.-Y., Madeleine, J.-B., Cheruy, F., Rochetin, N., Ghattas, J. (2020). LMDZ6: the improved atmospheric component of the IPSL coupled model. *J. Adv. Model. Earth Sys.*, 12 (6). doi:10.1029/2019MS001988.

Hu, A., Meehl, G. A., Han, W., & Yin, J. (2011). Effect of the potential melting of the Greenland Ice Sheet on the Meridional Overturning Circulation and global climate in the future. *Deep Sea Research Part II: Topical Studies in Oceanography*, 58(17-18), 1914-1926, doi:.10.1016/j.dsr2.2010.10.069

Hu, S., & Fedorov, A. V. (2019). Indian Ocean warming can strengthen the Atlantic meridional overturning circulation. *Nature climate change*, 9(10), 747-751, doi:10.1038/s41558-019-0566-x.

Hu, S., & Fedorov, A. V. (2020). Indian Ocean warming as a driver of the North Atlantic warming hole. Submitted.

Hurrell, J. W. (1995). Decadal trends in the North Atlantic Oscillation: regional temperatures and precipitation. *Science*, 269(5224), 676-679, doi:10.1126/science.269.5224.676.

Ihara, C., Kushnir, Y., & Cane, M. A. (2008). Warming trend of the Indian Ocean SST and Indian Ocean dipole from 1880 to 2004. *Journal of Climate*, 21(10), 2035-2046, doi:10.1175/2007JCLI1945.1.

Intergovernmental Panel on Climate Change (IPCC; 2013). In T. F. Stocker, et al. (Eds.), Climate change 2013: The physical science basis. Contribution of Working Group I to the Fifth Assessment Report of the Intergovernmental Panel on Climate Change (p. 1535). Cambridge, United Kingdom and New York: Cambridge University Press.

Jackson, L. C., Peterson, K. A., Roberts, C. D., & Wood, R. A. (2016). Recent slowing of Atlantic overturning circulation as a recovery from earlier strengthening. *Nature Geoscience*, *9*(7), 518-522,doi:10.1038/ngeo2715.

Jackson, L., & Wood, R. A. (2020). Fingerprints for Early Detection of Changes in the AMOC. *Journal of Climate*, *33*(16), 7027-7044, doi:10.1175/JCLI-D-20-0034.1.

Jackson, L., & Vellinga, M. (2013). Multidecadal to Centennial Variability of the AMOC: HadCM3 and a Perturbed Physics Ensemble. *Journal of Climate*, 26(7), 2390–2407, doi:10.1175/JCLI-D-11-00601.1

Jiang, W., Gastineau, G., & Codron, F. (2021). Multi-centennial variability driven by salinity exchanges between the Atlantic and the Arctic Ocean in a coupled climate model. *Journal of Advances in Modeling Earth Systems*, e2020MS002366, doi:10.1029/2020MS002366.

Kieke, D., Rhein, M., Stramma, L., Smethie, W. M., LeBel, D. A., & Zenk, W. (2006). Changes in the CFC inventories and formation rates of Upper Labrador Sea Water, 1997–2001. *Journal of Physical Oceanography*, 36(1), 64–86, doi:10.1175/JPO2814.1.

Krinner, G., Viovy, N., de Noblet-Ducoudr_e, N., Og_ee, J., Polcher, J., Friedlingstein, P., . . . Prentice, I. C. (2005). A dynamic global vegetation model for studies of the coupled atmosphere-biosphere system. *Global Biogeo. Cycles*, 19 (1), GB1015, doi:10.1029/2003GB002199.

Latif, M., Roeckner, E., Mikolajewicz, U., & Voss, R. (2000). Tropical stabilization of the thermohaline circulation in a greenhouse warming simulation. *Journal of Climate*, 13(11), 1809-1813, doi:10.1175/1520-0442(2000)013<1809:L>2.0.CO;2.

Lee, S., Gong, T., Johnson, N., Feldstein, S. B., & Pollard, D. (2011). On the possible link between tropical convection and the Northern Hemisphere Arctic surface air temperature change between 1958 and 2001. *Journal of Climate*, 24(16), 4350-4367, doi:10.1175/2011JCLI4003.1.

Lott, F., & Guez, L. (2013). A stochastic parameterization of the gravity waves due to convection and its impact on the Equatorial stratosphere. *J. Geophys. Res*., 118, 8897-8909, doi:10.1002/jgrd.50705

Liu, W., & Fedorov, A. V. (2019). Global impacts of Arctic sea ice loss mediated by the Atlantic meridional overturning circulation. *Geophysical Research Letters*, 46(2), 944-952, doi:10.1029/2018GL080602.

Liu, W., & Fedorov, A. V. (2020). Interaction between Arctic sea ice and the Atlantic meridional overturning circulation in a warming climate. *PNAS*, submitted.

Liu, W., Fedorov, A., & Sévellec, F. (2019). The mechanisms of the Atlantic meridional overturning circulation slowdown induced by Arctic sea ice decline. *Journal of Climate*, 32(4), 977-996, doi:10.1175/JCLI-D-18-0231.1.

Liu, W., Fedorov, A. V., Xie, S. P., & Hu, S. (2020). Climate impacts of a weakened Atlantic Meridional Overturning Circulation in a warming climate. *Science advances*, 6(26), eaaz4876, doi:10.1126/sciadv.aaz4876.

Liu, W., Xie, S. P., Liu, Z., & Zhu, J. (2017). Overlooked possibility of a collapsed Atlantic Meridional Overturning Circulation in warming climate. *Science Advances*, 3(1), e1601666, doi:10.1126/sciadv.1601666.

Madec, G., Bourdall_e-Badie, R., Bouttier, P., Bricaud, C., Bruciaferri, D., Calvert, D., & Vancoppenolle, M. (2017). NEMO ocean engine (version v3.6). *Notes du Pôle de modélisation de l'Institut Pierre-Simon Laplace (IPSL)*. doi:1598 10.5281/zenodo.1472492.

Marshall, J., Donohoe, A., Ferreira, D., & McGee, D. (2014). The ocean's role in setting the mean position of the Inter-Tropical Convergence Zone. *Climate Dynamics*, 42(7-8), 1967-1979, doi:10.1007/s00382-013-1767-z.

Menary, M. B., Park, W., Lohmann, K., Vellinga, M., Palmer, M. D., Latif, M., & Jungclaus, J. H. (2012). A multimodel comparison of centennial Atlantic meridional overturning circulation variability. *Climate dynamics*, *38*(11-12), 2377-2388, doi:10.1007/s00382-011-1172-4.

Mignot, J., de Boyer Montégut, C., Lazar, A., & Cravatte, S. (2007). Control of salinity on the mixed layer depth in the world ocean: 2. Tropical areas. *Journal of Geophysical Research: Oceans*, 112(C10), doi:10.1029/2006JC003954.

Mignot, J., & Frankignoul, C. (2010). Local and remote impacts of a tropical Atlantic salinity anomaly. *Climate dynamics*, 35(7-8), 1133-1147, doi:10.1007/s00382-009-0621-9.

Moreno-Chamarro, E., Marshall, J., & Delworth, T. L. (2020). Linking ITCZ Migrations to the AMOC and North Atlantic/Pacific SST Decadal Variability. *Journal of Climate*, 33(3), 893-905, doi:10.1175/JCLI-D-19-0258.1.

Msadek, R., & Frankignoul, C. (2009). Atlantic multidecadal oceanic variability and its influence on the atmosphere in a climate model. *Climate dynamics*, 33(1), 45-62, doi:10.1007/s00382-008-0452-0.

Olonscheck, D., Mauritsen, T., & Notz, D. (2019). Arctic sea-ice variability is primarily driven by atmospheric temperature fluctuations. *Nature Geoscience*, *12*(6), 430-434, doi:10.1038/s41561-019-0363-1.

898 Ortega, P., Mignot, J., Swingedouw, D., Sévellec, F., & Guilyardi, E. (2015). Reconciling two
899 alternative mechanisms behind bi-decadal variability in the North Atlantic. *Progress in*
900 *Oceanography*, 137, 237-249, doi:10.1016/j.pocean.2015.06.009.
901 Ortega, P., Robson, J., Sutton, R. T., & Andrews, M. B. (2017). Mechanisms of decadal
902 variability in the Labrador Sea and the wider North Atlantic in a high-resolution climate
903 model. *Climate Dynamics*, 49(7-8), 2625-2647, doi:10.1007/s00382-016-3467-y.
904 Park, H. S., Lee, S., Son, S. W., Feldstein, S. B., & Kosaka, Y. (2015). The impact of poleward
905 moisture and sensible heat flux on Arctic winter sea ice variability. *Journal of Climate*,
906 28(13), 5030-5040, doi:10.1175/JCLI-D-15-0074.1.
907 Rahmstorf, S. (2002). Ocean circulation and climate during the past 120,000
908 years. *Nature*, *419*(6903), 207-214, doi:10.1038/nature01090.
909 Rahmstorf, S., Box, J. E., Feulner, G., Mann, M. E., Robinson, A., Rutherford, S., &
910 Schaffernicht, E. J. (2015). Exceptional twentieth-century slowdown in Atlantic Ocean
911 overturning circulation. *Nature climate change*, 5(5), 475-480,
912 doi:10.1038/nclimate2554.
913 Rao, S. A., Dhakate, A. R., Saha, S. K., Mahapatra, S., Chaudhari, H. S., Pokhrel, S., & Sahu,
914 S. K. (2012). Why is Indian Ocean warming consistently?. *Climatic change*, 110(3),
915 709-719, doi:10.1007/s10584-011-0121-x.
916 Richter, I., & Xie, S. P. (2010). Moisture transport from the Atlantic to the Pacific basin and
917 its response to North Atlantic cooling and global warming. *Climate Dynamics*, 35(2-3),
918 551-566, doi:10.1007/s00382-009-0708-3.
919 Rousset, C., Vancoppenolle, M., Madec, G., Fichefet, T., Flavoni, S., Barthélemy, A., . . .
920 Vivier, F. (2015). The Louvain-La-Neuve sea ice model LIM3.6: global and regional
921 capabilities. *Geophys. Mod. Dev*., 28, 2991-3005. doi:1710 10.5194/gmd-8-2991-2015.
922 Roxy, M. K., Ritika, K., Terray, P., & Masson, S. (2014). The curious case of Indian Ocean
923 warming. *Journal of Climate*, 27(22), 8501-8509, doi:10.1175/JCLI-D-14-00471.1.
924 Sabine, C. L., Feely, R. A., Gruber, N., Key, R. M., Lee, K., Bullister, J. L., ... & Millero, F. J.
925 (2004). The oceanic sink for anthropogenic CO2. *Science*, 305(5682), 367-371,
926 doi:10.1126/science.1097403.
927 Seager, R., & Battisti, D. S. (2007). The Global Circulation of the Atmosphere. *Challenges to*
928 *our understanding of the general circulation: Abrupt climate change*, 331-371.
929 Sévellec, F., Fedorov, A. V., & Liu, W. (2017). Arctic sea-ice decline weakens the Atlantic
930 meridional overturning circulation. *Nature Climate Change*, 7(8), 604-610,
931 doi:10.1038/NCLIMATE3353.
932 Smeed, D.A., Josey, S.A., Beaulieu, C., Johns, W.E., Moat, B.I., Frajka-Williams, E., Rayner,
933 D., Meinen, C.S., Baringer, M.O., Bryden, H.L. and McCarthy, G.D. (2018). The North
934 Atlantic Ocean is in a state of reduced overturning. *Geophysical Research Letters*,
935 45(3), 1527-1533, doi:10.1002/2017GL076350.
936 Speer, K., Guilyardi, É., & Madec, G. (2000). Southern Ocean transformation in a coupled
937 model with and without eddy mass fluxes. *Tellus A*, 52(5), 554-565,
938 doi:10.1034/j.1600-0870.2000.01060.x.
939 Speer, K., Tziperman, E. (1992) rates of water mass formation in the North Atlantic Ocean. *J*
940 *Phys Oceanogr,* 22(1), 93–104, doi:10.1175/1520-0485(1992)022<0093:ROWMF
941 I>2.0.CO;2
942 Sutton, R. T., & Hodson, D. L. (2005). Atlantic Ocean forcing of North American and
943 European summer climate. *Science*, 309(5731), 115-118,
944 doi:10.1126/science.1109496.
945 Swingedouw, D., Braconnot, P., Delécluse, P., Guilyardi, E., & Marti, O. (2007). Quantifying
946 the AMOC feedbacks during a 2× CO 2 stabilization experiment with land-ice melting.
947 *Climate Dynamics*, 29(5), 521-534, doi:10.1007/s00382-007-0250-0.

948 Thomas, M. D., & Fedorov, A. V. (2019). Mechanisms and impacts of a partial AMOC
949 recovery under enhanced freshwater forcing. *Geophysical Research Letters*, 46(6),
950 3308-3316, doi:10.1029/2018GL080442.
951 Trenberth, K. E., Branstator, G. W., Karoly, D., Kumar, A., Lau, N. C., & Ropelewski, C.
952 (1998). Progress during TOGA in understanding and modeling global teleconnections
953 associated with tropical sea surface temperatures. *Journal of Geophysical Research:*
954 *Oceans*, 103(C7), 14291-14324, doi:10.1029/97JC01444.
955 Vancoppenolle, M., Fichefet, T., Goosse, H., Bouillon, S., Madec, G., & Morales Maqueda,
956 M. A. (2009). Simulating the mass balance and salinity of Arctic and Antarctic sea ice.
957 1. Model description and validation. *Ocean Modelling*, 27, 54-69.
958 doi:10.1016/j.ocemod.2008.11.003.
959 Vellinga, M., & Wood, R. A. (2002). Global climatic impacts of a collapse of the Atlantic
960 thermohaline circulation. *Climate Change*, 54(3), 251-267,
961 doi:10.1023/A:1016168827653.
962 Vellinga, M., & Wu, P. (2004). Low-Latitude Freshwater Influence on Centennial Variability
963 of the Atlantic Thermohaline Circulation. Journal of Climate, 17(23), 4498–4511,
964 doi:10.1175/3219.1
965 Watt-Meyer, O., & Frierson, D. M. (2019). ITCZ width controls on Hadley cell extent and
966 eddy-driven jet position and their response to warming. *Journal of Climate*, 32(4),
967 1151-1166, doi:10.1175/JCLI-D-18-0434.1.
968 Walin, G. (1982). On the relation between sea–surface heat flow and thermal circulation in the
969 ocean. *Tellus* 34(2), 187–195, doi:10.3402/tellu sa.v34i2 .10801.
970 Woollings, T., Gregory, J. M., Pinto, J. G., Reyers, M., & Brayshaw, D. J. (2012). Response
971 of the North Atlantic storm track to climate change shaped by ocean-atmosphere
972 coupling. *Nature Geoscience*, 5(5), 313-317 doi:10.1038/ngeo1438.
973 Worthington, E. L., Moat, B. I., Smeed, D. A., Mecking, J. V., Marsh, R., & McCarthy, G. D.
974 (2021). A 30-year reconstruction of the Atlantic meridional overturning circulation
975 shows no decline. *Ocean Science*, 17(1), 285-299, doi:10.5194/os-17-285-2021.
976 Zhang, J., & Zhang, R. (2015). On the evolution of Atlantic meridional overturning circulation
977 fingerprint and implications for decadal predictability in the North Atlantic.
978 *Geophysical Research Letters*, 42(13), 5419-5426, doi:10.1002/2015GL064596.
979 Zhang, R. (2008). Coherent surface-subsurface fingerprint of the Atlantic meridional
980 overturning circulation. *Geophysical Research Letters*, 35(20), doi:
981 10.1029/2008GL035463.

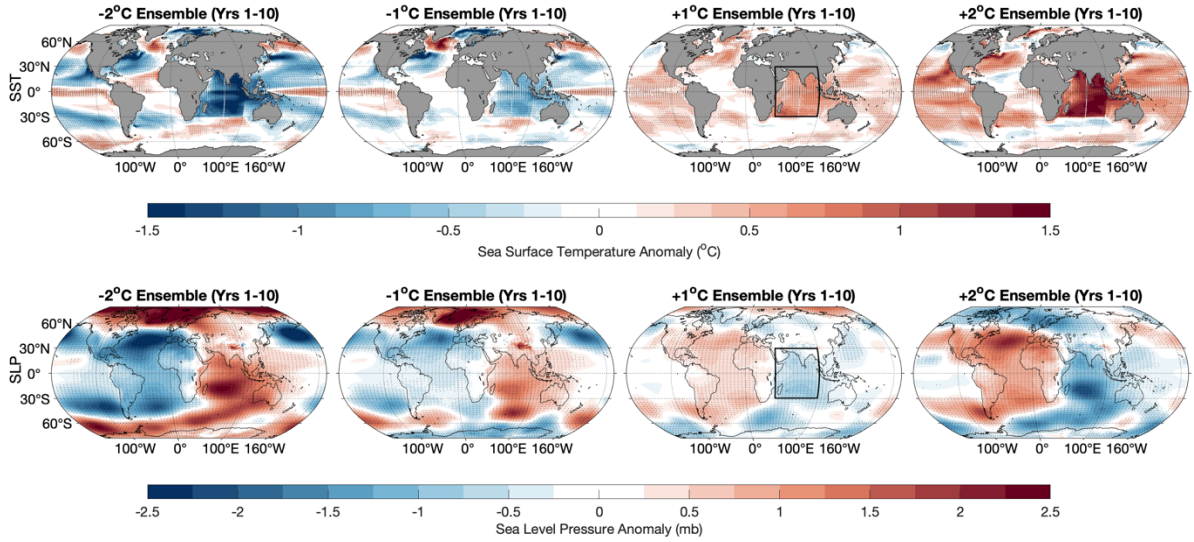

Fig. 1 Anomalies of SST (top row) and sea level pressure (bottom row) averaged for years 1-10 in the -2, -1, +1, and +2ºC TIO surface temperature nudging experiments, representing the initial response to the imposed forcing. The black box marks the area of the tropical Indian Ocean (TIO) where the nudging is applied. Note that the actual changes in TIO SST are smaller than the imposed targets, reaching roughly -1.4, -0.7, +0.7, and +1.4 respectively. Also note an NAO-like pattern in SLP and SST changes in the North Atlantic.

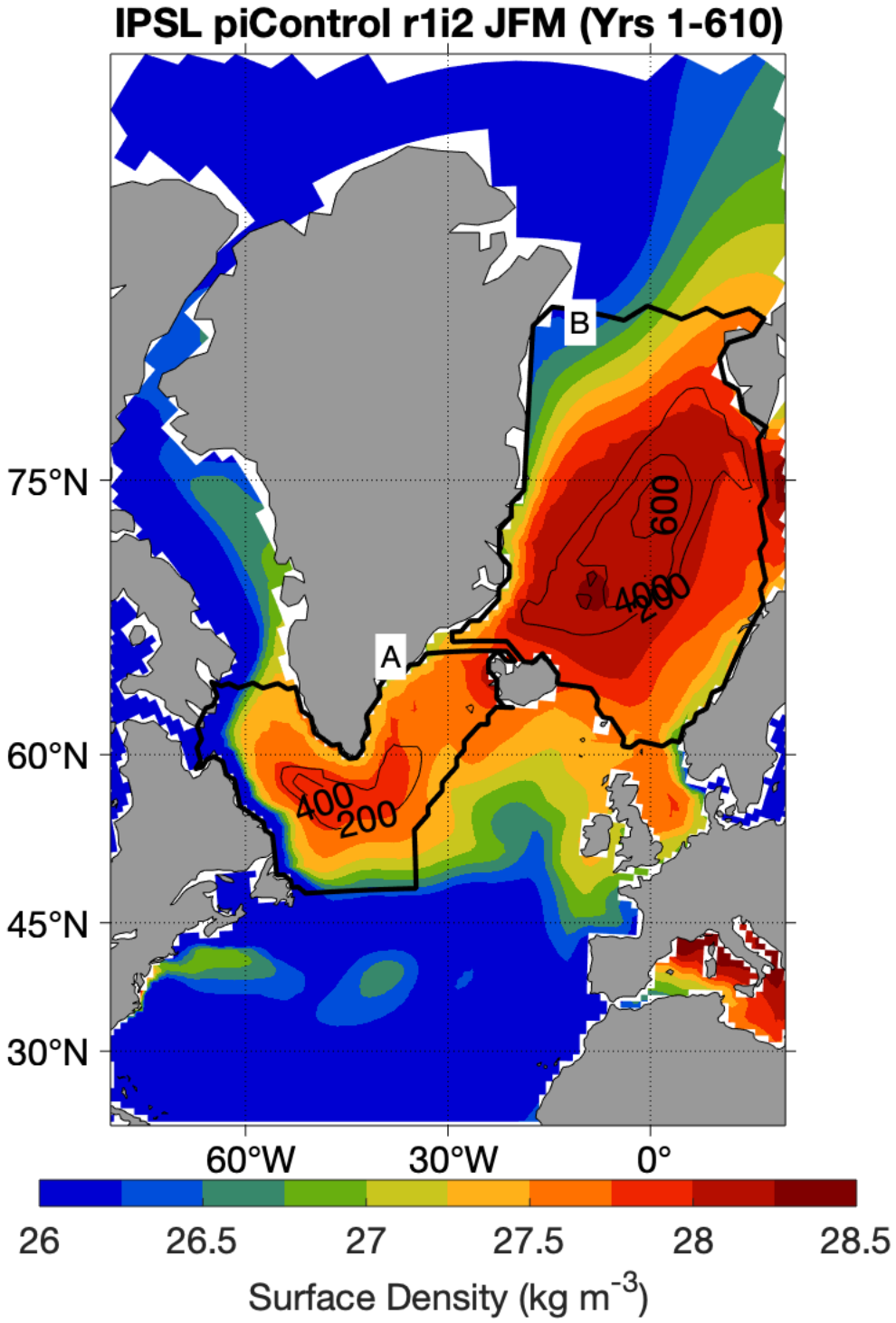

Fig. 2 Mean winter (January-March) neutral density at the surface (colors, kg m^{-3}) and standard deviation of mixed layer depth (light contours, m) in the control simulation. The deep convective regions are separated into two areas as marked by heavy black contours. The separation is based on bathymetric features, surface density, and winter mixed layer depth variability. Region A corresponds to the extended Labrador Sea area that includes the Irminger sea, and region B to the Nordic Seas.

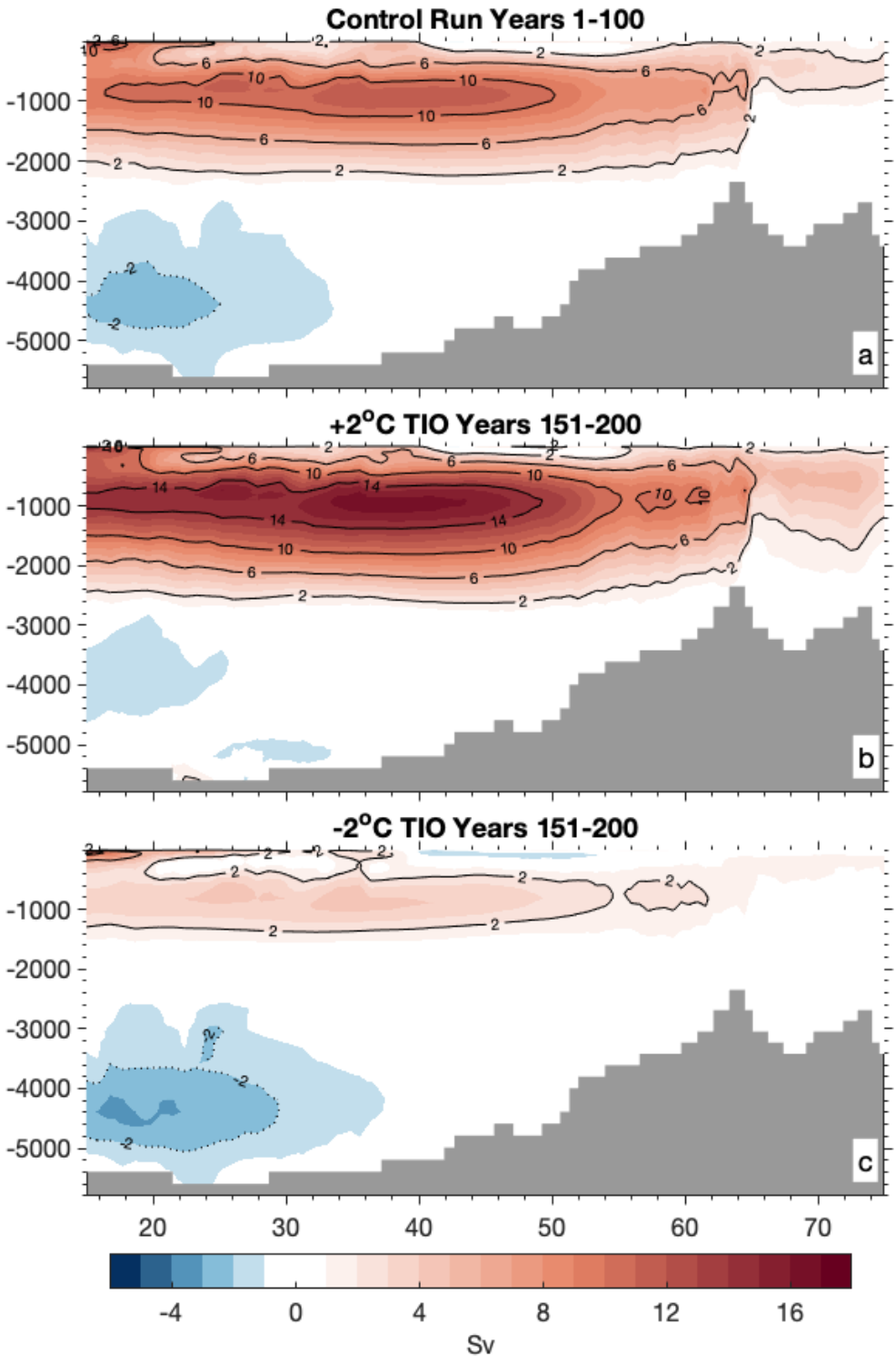

Fig. 3 Ensemble mean zonally-averaged meridional overturning circulation within the Atlantic basin (Sv) in (a) the control run years 1-100, and in (b) TIO +2°C and (c) TIO -2°C experiments for years 151-200. The latter period represents a quasi-equilibrium for the two perturbation experiments, even though the ocean continues to adjust slowly especially in the -2°C experiment wherein the AMOC will eventually collapse after some 300 years.

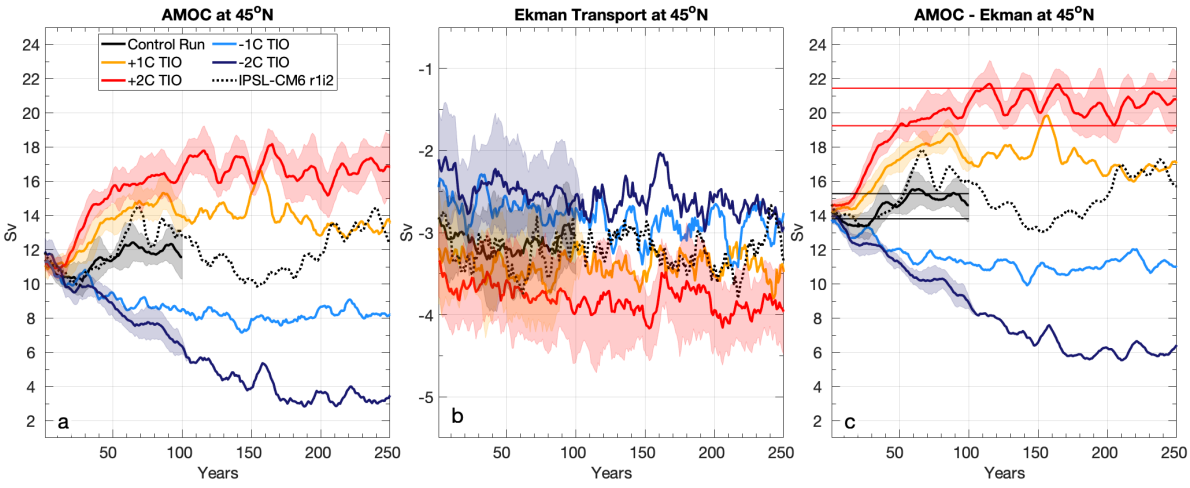

Fig. 4 Time-series of maximum AMOC strength at 45°N, meridional Ekman transport, and the meridional overturning index (AMOC minus Ekman), all in units of Sv, for different experimetns. An 11-year moving mean has been applied; shading indicates ensemble spread (when available). The light horizontal gray and red lines in the right panel represent the 100-year 95% confidence interval of the control experiment and the year 100-250 95% confidence interval of the +2°C-TIO experiment.

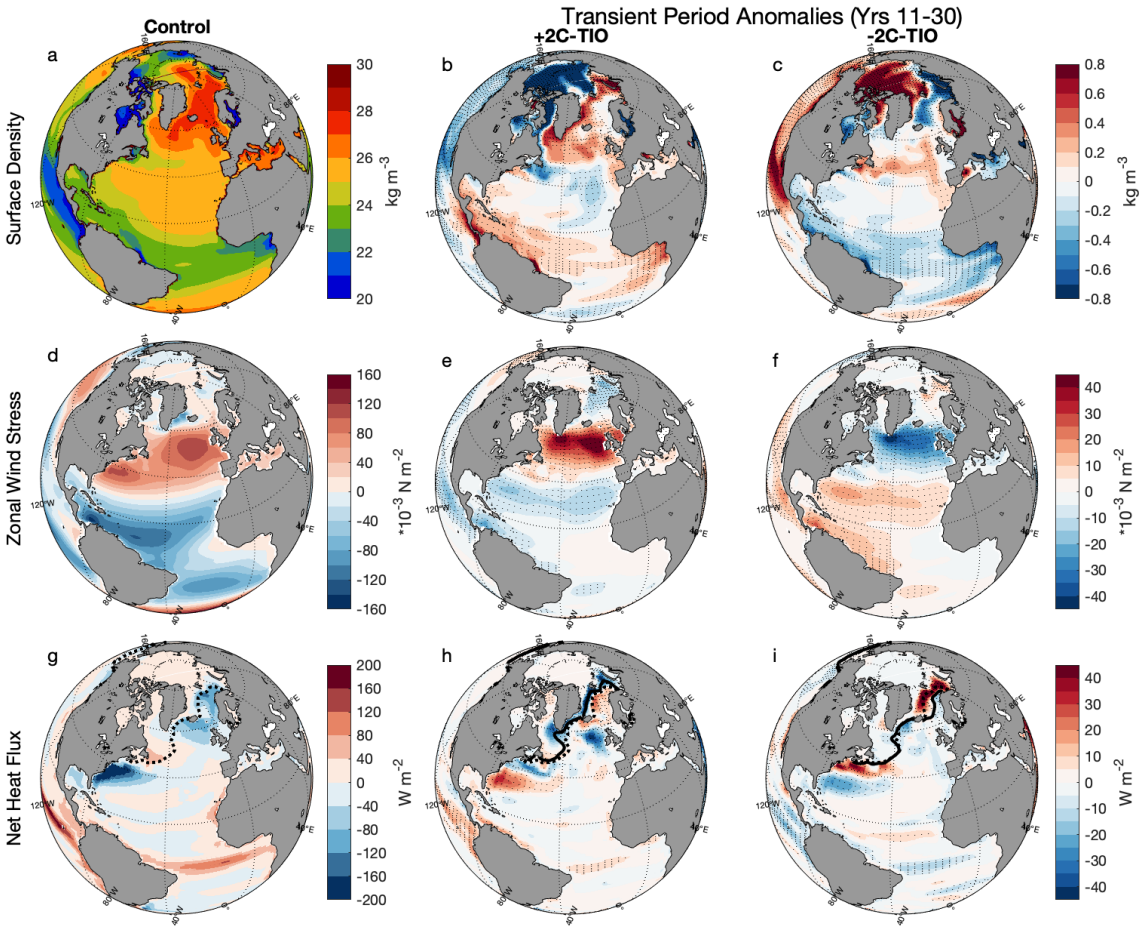

Fig. 5 Mean surface fields in the control simulations (left column) and the initial Atlantic Ocean response to the TIO forcing during years 11-30 in the TIO+2ºC (middle column; b, e, and h) and -2ºC (right column; c, f, and i) experiments. Panels (b, c) show neutral density anomalies (kg/m^3), (e, f) are anomalies in zonal wind stress (N m^{-2}), and (h, i) are anomalies in net heat flux (W m^{-2}). Positive net heat fluxes are into the ocean (g). Also shown is winter sea ice extent in the control and perturbation experiments (dashed and solid black contours, respectively), defined as the boundary corresponding to 15% sea ice concentration. Anomalies exceeding the 95% confidence interval of the piControl r1i2 are stippled.

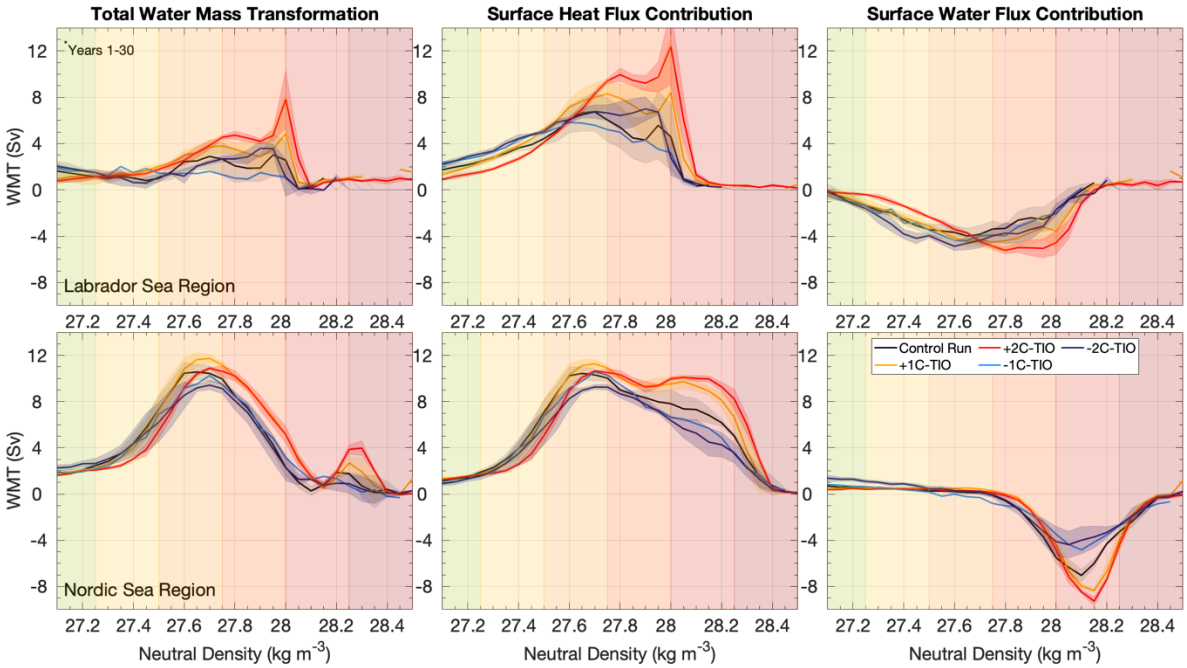

Fig. 6 Total water mass transformation rates (WMT, Sv) within the Labrador and Nordic Seas regions during the initial period, and contributions to WMT from heat and fresh water fluxes (Sv). Averages for years 11-30 are shown. The data are binned in 0.05 kg m^{-3} neutral density classes. Shading represents the 3-member ensemble spread. Background colors correspond to the surface densities in figure 2.

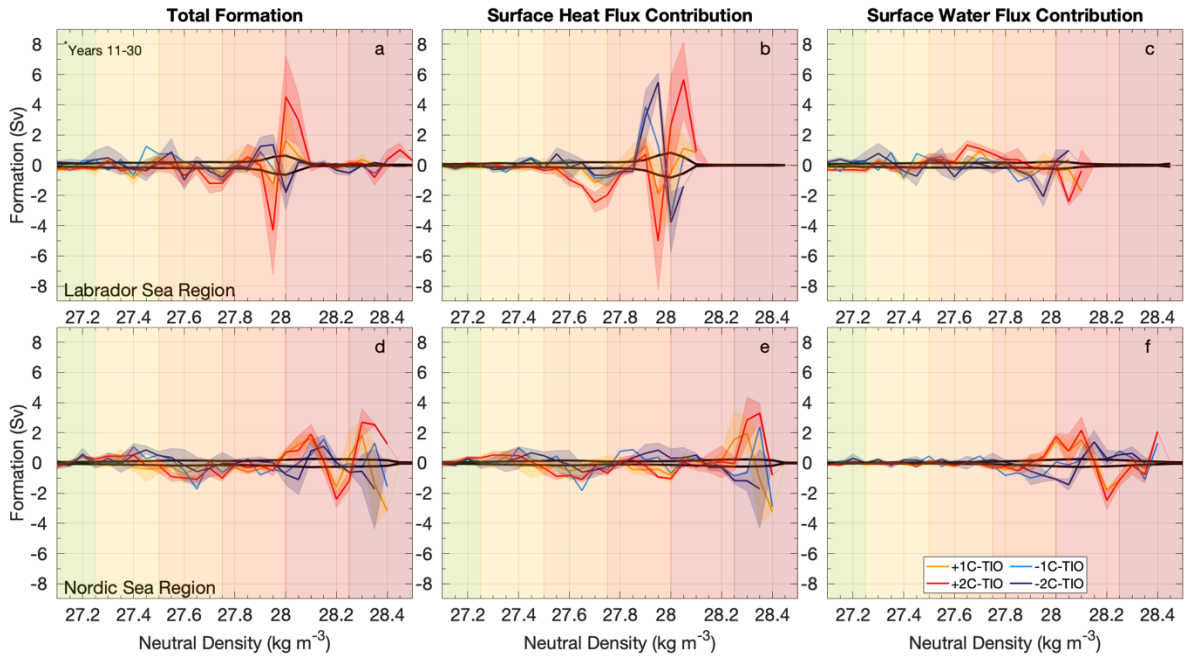

Fig. 7 Anomalous dense water formation, summed in 0.05 kg m^{-3} neutral density bins, for the Labrador and Nordic Seas regions. Averages for years 11-30 are shown. Formation rates are computed as the divergence of water mass transformation rates (WMT) with respect to density. The total formation is the sum of the surface heat and fresh water flux contributions. Background colors correspond to the surface densities in Figure 2. The black lines represent the 95% confidence interval of dense water formation within the control experiment. Note the increase (decrease) of dense water formation in the warm (cold) TIO perturbation experiments.

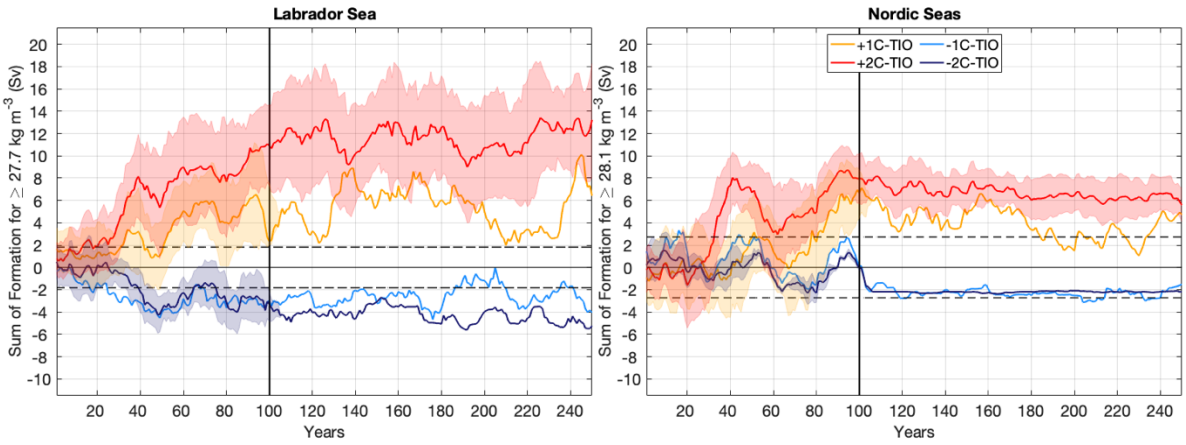

Fig. 8 Time-series of year-to-year anomalous dense water formation in the Labrador (density bins ≥ 27.8 kg m^{-3}) and Nordic Seas (density bins ≥ 28.1 kg m^{-3}) regions, relative to the control run. An 11-year moving mean has been applied; shading indicates ensemble spread. The density ranges were selected from Figure 7 and represent the approximate anomalous contributions to the formation of North Atlantic Deep-water, respectively, from the two regions. Note that in the -1 and -2°C TIO experiments after year 100. After the vertical black line, the 100-yr ensemble time mean of the control run is used to compute anomalies.

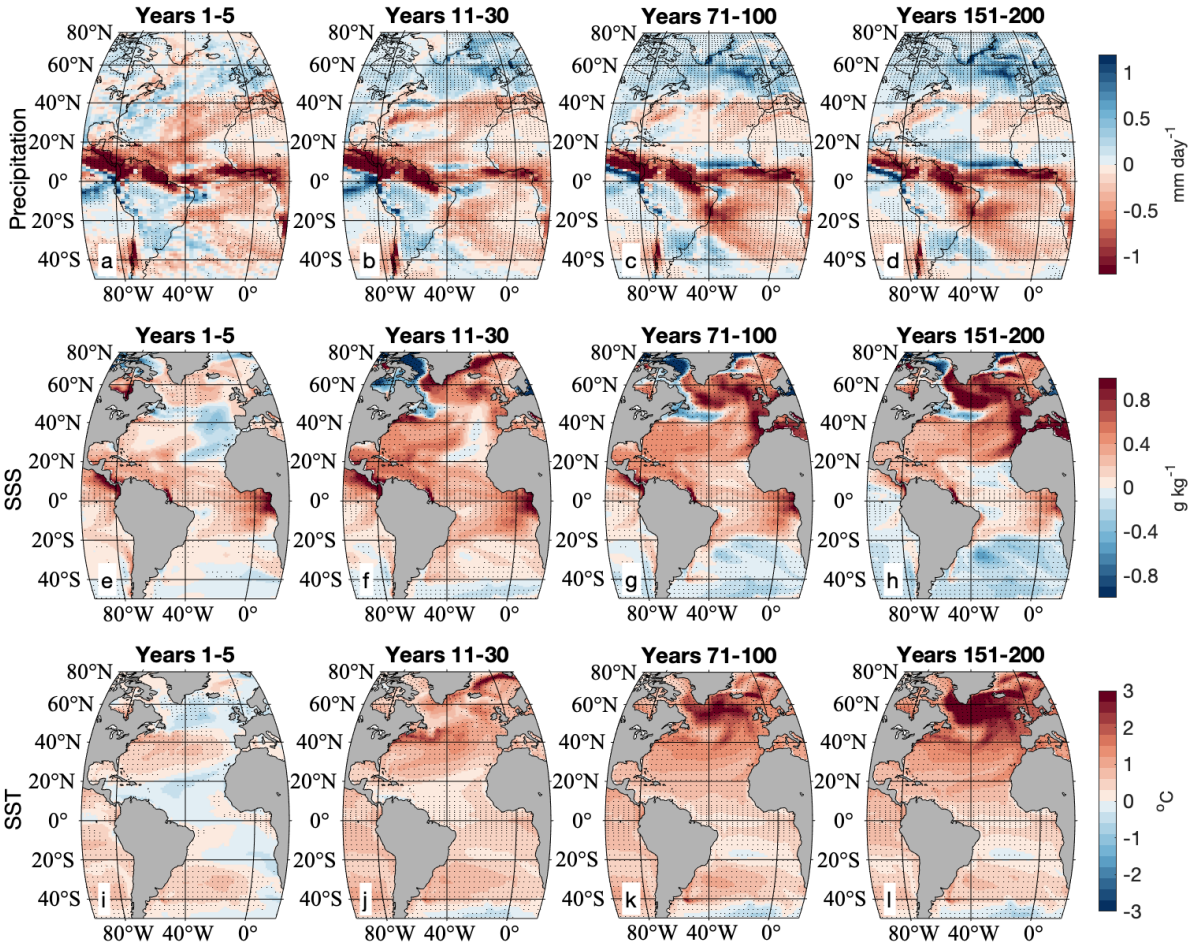

Fig. 9 Anomalies of (a-d) precipitation, (e-h) sea surface salinity (SSS), and (i-l) SST for different time intervals within the Atlantic basin for the +2°C TIO experiments. Speckled patches within the spatial plots represent the anomalies larger than the 610-year 95%-confidence intervals of the IPSL-CM6 r1i2. These plots depict the "slow" mechanism of the AMOC changes associated with the advection of positive salinity anomalies from the tropical Atlantic Basin to the subpolar North Atlantic. These salinity anomalies are largely caused by anomalously low precipitation in the tropical and subtropical Atlantic and then amplified by the salt-advection feedback.

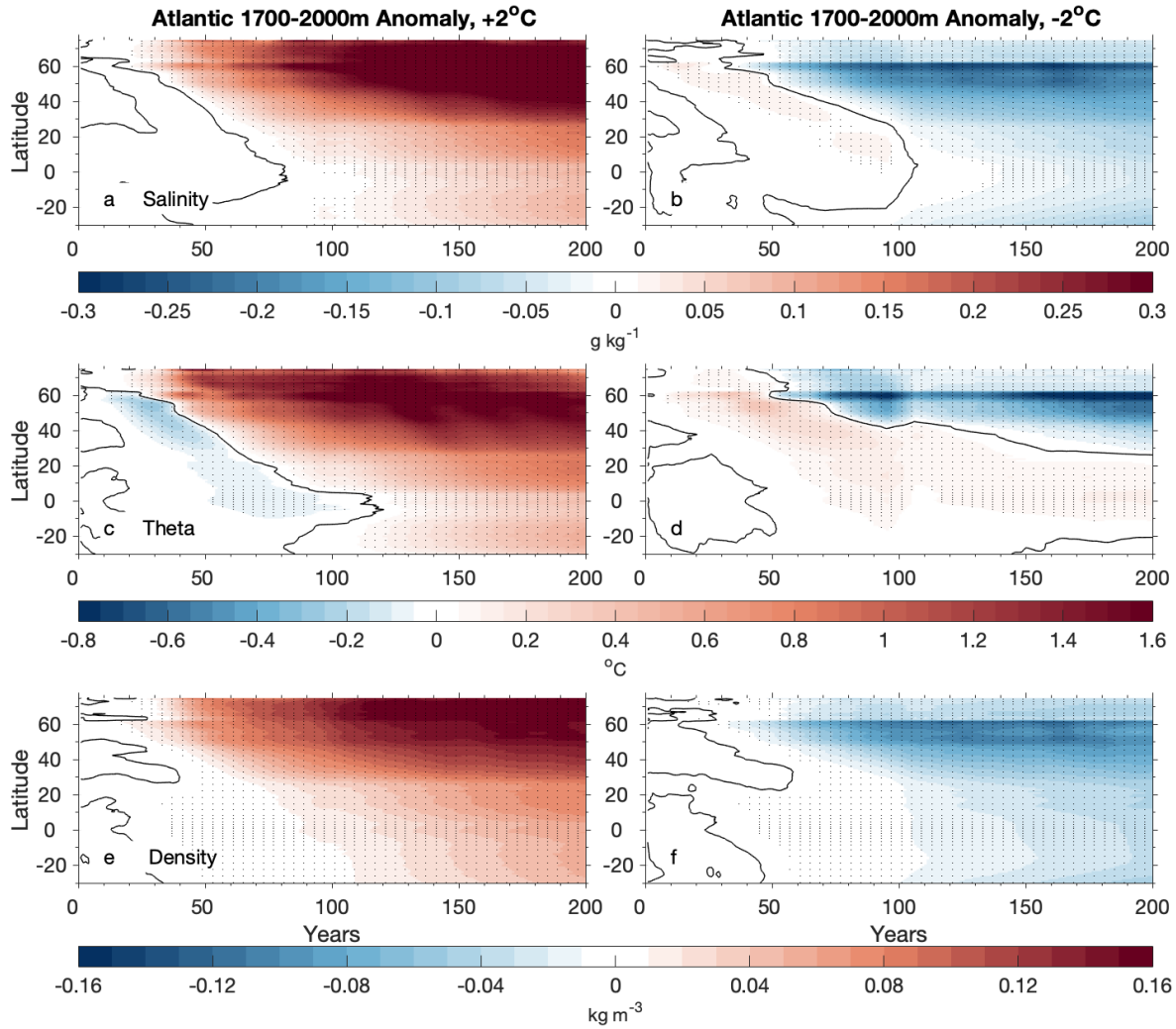

Fig. 10 Hovmoller diagrams showing anomalies of zonally averaged (a,b) salinity, (c,d) temperature, and (e,f) density, all averaged between 1700-2000m depth within the Atlantic basin, for the +2°C (left) and -2°C (right) TIO experiments. Black contours represent zero values. Note that the density anomalies are dominated by temperature in the fast response, but salinity in the slow response.

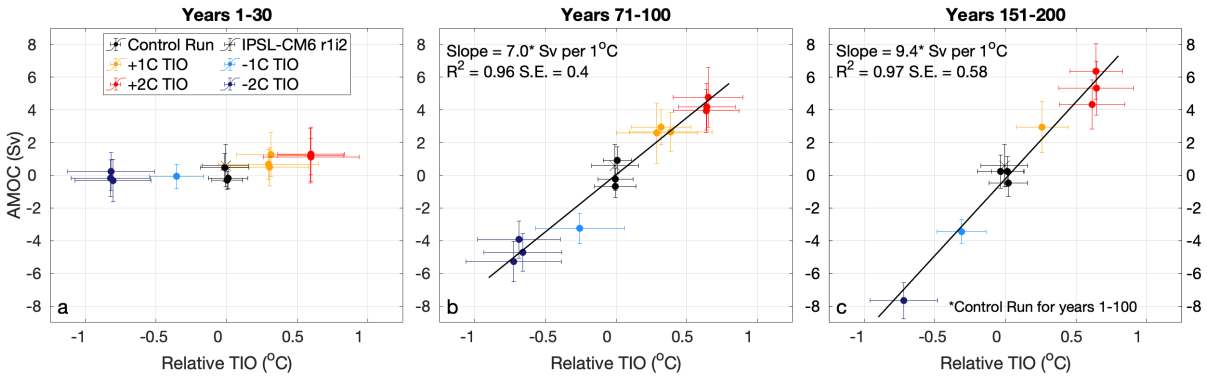

Fig. 11 Anomalies of the AMOC intensity at 45°N versus the TIO relative SST in different experiments for years (a) 1-30, (b) 71-100, and (c) 151-200. Dots of the same color represent time-mean averages for different ensemble members within a particular experiment. The error bars represent the standard deviation of annual means. An additional control run (IPSL-CM6 piControl r1i2) is included for comparison. Both horizontal and vertical axes are relative to our mean control ensemble, positioning the control run to zero. Panels (b) and (c) also show a linear least-squares fit. The linear regression is significant at alpha = 0.05 ($p < 0.001$). The regression (slope), coefficient of determination (R^2), and standard error (S.E.) are included for the regression line.